ELEMENTA
Science of the Anthropocene

Dmitrenko, IA, et al. 2020. Atmospheric vorticity sets the basin-scale circulation in Hudson Bay. *Elem Sci Anth*, 8: XX. DOI: https://doi.org/10.1525/elementa.049

RESEARCH ARTICLE

Atmospheric vorticity sets the basin-scale circulation in Hudson Bay

Igor A. Dmitrenko[1,*], Paul G. Myers[2], Sergei A. Kirillov[1], David G. Babb[1], Denis L. Volkov[3,4], Jennifer V. Lukovich[1], Ran Tao[2], Jens K. Ehn[1], Kevin Sydor[5], and David G. Barber[1]

Hudson Bay of northern Canada receives upward of 700 km^3 of river discharge annually. Cyclonic water circulation in Hudson Bay transports this massive volume of riverine water along the coast toward Hudson Strait and into the Labrador Sea. However, synoptic, seasonal and interannual variability of the freshwater transport in Hudson Bay remains unclear. Using yearlong observations of current velocity profiles, collected from oceanographic moorings deployed in western Hudson Bay from September 2016 to September/October 2017, we examined the role of atmospheric forcing on circulation and freshwater transport in the Bay. Our analysis reveals that the along-shore southeastward current through western Hudson Bay was amplified through the entire water column in response to winds generated by cyclones passing over Hudson Bay toward Baffin Bay and/or the Labrador Sea. An atmospheric vorticity index was used to describe the atmospheric forcing and found to correlate with sea surface height and along-shore currents. We showed that a surface Ekman on-shore transport increases sea surface heights along the coast, producing a cross-slope pressure gradient that drives an along-shore southeastward flow, in the same direction as the wind. Expanding our observations to the bay-wide scale, we confirmed this process of wind-driven water dynamics with (1) satellite altimetry measurements and (2) ocean model simulations. Ultimately, we find that cyclonic wind forcing amplifies cyclonic water circulation in Hudson Bay facilitating the along-shore freshwater transport to Hudson Strait. During periods of positive atmospheric vorticity, this forcing can reduce the residence time of riverine water in Hudson Bay.

Keywords: Hudson Bay, velocity measurements, cyclonic water circulation, wind forcing, atmospheric vorticity

Introduction

Hudson Bay is a large ($\sim$ 831,000 km^2), shallow (mean depth of $\sim$ 150 m), semi-enclosed subarctic inland sea connected to the Labrador Sea through Hudson Strait (**Figure 1**). Hudson Bay is seasonally covered by a dynamic ice cover from November/December to June/July (Hochheim and Barber, 2011, 2014) with a mean ice thickness in April ranging from 1.2 m to 1.7 m from western to eastern Hudson Bay (Landy et al., 2017). Predominantly westerly winds advect the ice cover from west to east across the Bay, creating a large recurrent polynya in western Hudson Bay and a thicker, deformed ice cover in eastern Hudson Bay (Landy et al., 2017; Kirillov et al., 2020).

Oceanic water masses flowing into Hudson Bay are predominantly Arctic waters of Pacific origin (e.g., Prinsenberg, 1986a; Jones and Anderson, 1994; Ingram and Prinsenberg, 1998) that enter Hudson Bay through one of two gateways: (i) from the north through Fury and Hecla Strait via Foxe Basin, or (ii) from the east through Hudson Strait (**Figure 1a**). The local water mass of Hudson Bay is dominated by freshwater input comprised of river runoff from the largest watershed in Canada and sea-ice meltwater (e.g., Prinsenberg, 1984, 1988, 1991; Saucier and Dionne, 1998; Granskog et al., 2009; Eastwood et al., 2020). The annual mean discharge rate of 22.6 $\times$ 10^3 m^3 s^{-1} corresponds to a net discharge of 712 km^3 of freshwater per year (Déry et al., 2005, 2011), which allows us to consider Hudson Bay as a large-scale subarctic estuarine system. In terms of export, Hudson Strait is the only export pathway and transports $\sim$ 1,000 km^3 of freshwater per year to the Labrador Sea (Saucier et al., 2004), impacting the Labrador Current and downstream shelves (e.g., Myers et al., 1990). Overall, freshwater outflow from Hudson Bay is comparable to the total freshwater flux from the Greenland ice

[1] Centre for Earth Observation Science, University of Manitoba, Winnipeg, Manitoba, Canada
[2] Department of Earth and Atmospheric Sciences, University of Alberta, Edmonton, Alberta, Canada
[3] Cooperative Institute for Marine and Atmospheric Studies, University of Miami, Miami, FL, USA
[4] NOAA, Atlantic Oceanographic and Meteorological Laboratory, Miami, FL, USA
[5] Manitoba Hydro, Winnipeg, Manitoba, Canada
* Corresponding author:
Email: igor.dmitrenko@umanitoba.ca

sheet of ~ 1,300 km^3 year^{-1} (Bamber et al., 2018). Freshwater transport in Hudson Bay exhibits a strong seasonal cycle, which is due to the timing of river discharge (e.g., Déry et al., 2005), the annual melt/freeze cycle of sea ice (Ingram and Prinsenberg, 1998; Saucier et al., 2004; Straneo and Saucier, 2008), and the seasonality in wind forcing (Saucier et al., 2004; St-Laurent et al., 2011).

The mean circulation in Hudson Bay is comprised of the wind-driven and estuarine components, where the estuarine portion is driven by the riverine water input (Prinsenberg, 1986a). Cyclonic circulation of water within Hudson Bay was first reported by Hachey (1935) based on drift bottles released during the Hudson Bay Fisheries Expedition of 1930. Using data from summer cruises in 1975, 1976, and 1982, Prinsenberg (1986b) revealed that cyclonic circulation during summer was driven by wind forcing and that the monthly mean velocity was ~ 5 cm s^{-1}. Presently, Hudson Bay circulation is commonly accepted to be driven primarily by wind and to be cyclonic through the entire water column (e.g., Ingram and Prinsenberg, 1998; Saucier et al., 2004; St-Laurent et al., 2011, 2012; Ridenour et al., 2019a). Model simulations by Saucier et al. (2004) show that the cyclonic circulation is stronger during fall with a maximum in November when the winds are strongest, and weakest during spring when Hudson Bay has a complete sea-ice cover. Recently, Ridenour et al. (2019b) reported that summer circulation is more complex, with river discharge into southern Hudson Bay leading to the development of small-scale circulation features that are thermohaline-driven and anti-cyclonic.

While significant progress has been achieved in understanding the Hudson Bay environmental system (e.g., Granskog et al., 2009; Kuzyk et al., 2011; Kuzyk and Candlish, 2019; Eastwood et al., 2020), Hudson Bay still remains one of the least studied subarctic regions due to a scarcity of year-round *in situ* oceanographic observations. In 2016, the University of Manitoba and Manitoba Hydro launched a project on "Variability and change of freshwater-marine coupling in the Hudson Bay System", named BaySys, which aimed to assess the relative contributions of climate change and river regulation to the Hudson Bay system. The role of freshwater in Hudson Bay was investigated through field-based research coupled with climatic-hydrological-oceanographic-biogeochemical modeling that will be covered within this special feature. To further our knowledge of water dynamics within Hudson Bay, oceanographic moorings, equipped with velocity profilers, were deployed in western Hudson Bay from September 2016 to September/October 2017 (**Figures 1** and **2**). Mooring AN01 was deployed to assess oceanographic conditions upstream of the Nelson River estuary (**Figure 1**), whereas moorings NE02 and NE03 were placed in the mid- and outer parts of the Nelson River Estuary to evaluate oceanographic implications of the Nelson River regulation and their interplay with Hudson Bay circulation. Based on these year-long oceanographic observations, we explored the details of wind-driven water dynamics in the region. Satellite altimetry data and model simulations allowed us to expand our findings to the Bay-scale. Here we specifically build on the suggestion by Barber and Sydor (2014) that wind patterns directly impact the strength of the Hudson Bay boundary current.

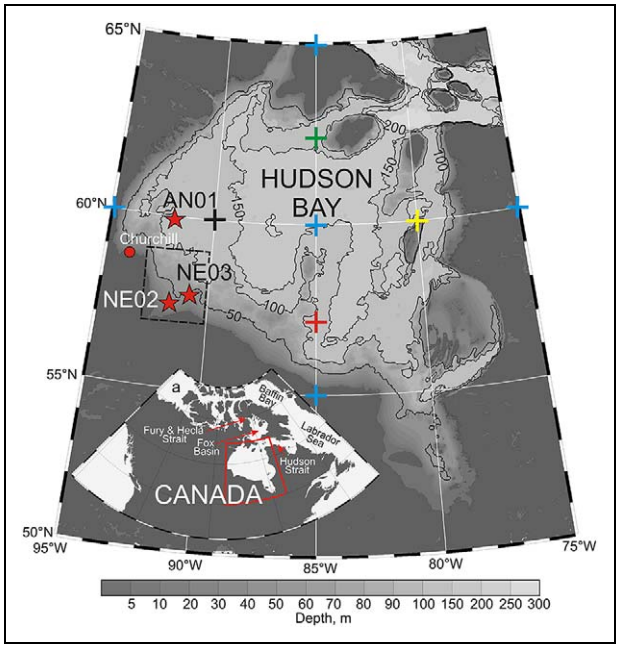

Figure 1. Map of Hudson Bay with location of the moorings. AN01, NE02 and NE03 moorings depicted with red stars. Red dot indicates the tide gauge at Churchill. Inset shows the Hudson Bay location in northern Canada. Blue crosses depict 5-point stencil used for computing Laplacian from sea level atmospheric pressure at 60°N, 85°W. Black, green, yellow and red crosses depict additional central nodes of the 5-point stencil used for estimating the sensitivity of Laplacian approximation. The numbered black lines depict depth contours of 50, 100, 150 and 200 m. The black dashed rectangle encloses the Nelson River estuary and adjoining western Hudson Bay enlarged in **Figure 2**. DOI: https://doi.org/10.1525/elementa.049.f1

Data

Year-long time-series measurements of velocity and internal pressure collected from two up-looking 300 kHz Workhorse Sentinel acoustic Doppler current profilers (ADCPs) by Teledyne RD Instruments (RDI) were used within this work. ADCPs were deployed on bottom-anchored moorings AN01 and NE03 located along the western coast of Hudson Bay (**Figure 1**). AN01 (59°58.2′N, 91°57.1′W, 107-m water depth) was deployed from September 27, 2016 to October 30, 2017 ~ 180 km northeast of Churchill. NE03 (57°49.8′N, 90°52.3′W, 52-m water depth) was deployed from September 28, 2016 to October 28, 2017 at approximately 150 km from the Nelson River mouth and 250 km southeast of AN01. ADCPs were placed at depths of 104 m and 49 m depth on AN01 and NE03, respectively. A similar setup was deployed at NE02 (57°30′N, 91°48′W, 44-m water depth, ~ 70 km to the Nelson River mouth; **Figures 1** and **2**), but the ADCP flipped during deployment and prevented the collection of velocity data; however, we still used the internal pressure time series. The velocity

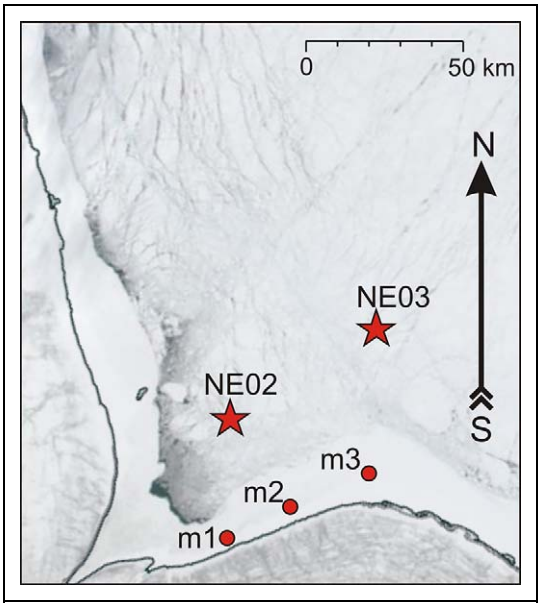

Figure 2. MODIS satellite imagery with location of the moorings in the Nelson River estuary. Positions of year-long (NE02 and NE03, red stars) and short-term (February–April 2017, m1–m3, red dots) moorings deployed in the Nelson River estuary and adjoining western Hudson Bay. MODIS satellite imagery is for March 14, 2017. The band of white ice along the coast corresponds to the landfast ice. The mobile ice pack is located off-shore of the landfast ice, with black areas of open water and areas of new ice (light grey) intermixed within the thicker pack ice (white floes). DOI: https://doi.org/10.1525/elementa.049.f2

data from the ADCPs were obtained at 2-m depth intervals, with a 15-min ensemble time interval and 15 pings per ensemble. The first bin was located at 4 m above the transducer. According to the manufacturer's estimates, the RDI ADCP precision and resolution are $\pm$ 0.5% and $\pm$ 0.1 cm s^{-1}, respectively. Its compass accuracy is $\pm$ 2°, and it was corrected by adding magnetic deviation. The velocity time series from AN01 was used previously by Petrusevich et al. (2020) for assessing patterns of the zooplankton diel vertical migration in response to tidal dynamics.

Measurements of sea level were obtained from three different sources: (1) the hourly tide gauge data from the port of Churchill (**Figure 1**); (2) sea level pressure data from ADCPs at AN01, NE02, and NE03; and (3) RBRsolo sea level data loggers temporarily deployed near the Nelson Estuary during winter 2017 (**Figure 2**). The RBR data loggers were deployed from February to April 2017 on the seafloor below landfast sea ice at water depths of 3.5–7.5 m at three landfast ice-tethered mooring sites (m1, m2, and m3; **Figure 2**). The RBRsolo pressure sensors have an accuracy of $\pm$ 0.05%. The specified short-term uncertainty of the ADCP internal pressure sensor is $\pm$ 0.1% of full scale range which is 200 m (Teledyne Marine, personal communication). For interpreting Churchill tide gauge data, we used the daily data on the Churchill River discharge above Red Head Rapids for 2016–2017, as retrieved from https://wateroffice.ec.gc.ca.

In addition, satellite altimetry data were used to expand our analysis of the relationship between atmospheric forcing and sea level changes. Daily maps of sea surface height (SSH) and geostrophic velocity anomalies relative to a 20-year mean sea surface were retrieved from the Copernicus Marine Environment Monitoring Service (https://marine.copernicus.eu). This dataset only exists during the open water season. Mean fields of SSH and geostrophic velocity anomalies were calculated to contrast a period of anticyclonic forcing during August 2017 with a period of cyclonic forcing during early September 2017.

Fields of sea level atmospheric pressure (SLP) and 10-m wind velocity at 6-h intervals were obtained from the National Centers for Environmental Prediction (NCEP; Kalnay et al., 1996). Cyclones over the Hudson Bay area were manually tracked using the NCEP SLP fields, with the central position and low SLP tabulated. The horizontal resolution of the NCEP-derived data is 2.5° of latitude. Hourly observations of wind and atmospheric pressure, retrieved from the Churchill airport meteorological station (location in **Figure 1**) through https://climate.weather.gc.ca/historical_data/search_historic_data_e.html, were used to validate NCEP data (**Figure 3**). Overall the zonal and meridional wind speeds and atmospheric pressure from the Churchill weather station and NCEP are strongly correlated ($k = 0.87$, 0.92, and 0.89, respectively; **Figure 3**). On average, NCEP underestimated the measured wind speed by 1.15 $\pm$ 1.61 m s^{-1}, but overestimated SLP by 2.54 $\pm$ 4.21 mbar (**Figure 3c**). Furthermore, the monthly-mean NCEP data at AN01 were compared to ERA5 (Copernicus Climate Change Service, 2017) data using the Web-Based Reanalysis Intercomparison Tools (WRIT) described by Smith et al. (2014a). ERA5 succeeds the ERA-Interim Reanalysis from the European Center for Medium-Range Weather Forecasts (Dee et al., 2011; Hoffmann et al., 2019). At AN01 from October 2016 to September 2017, NCEP wind speeds slightly exceeded ERA5 by 0.05 and 0.06 m s^{-1} for zonal and meridional wind, respectively, while SLP was 0.99 mbar greater in ERA5 than in NCEP.

Methods

For the 2016–2017 study period a vorticity index was derived from the daily mean SLP NCEP data to characterize the atmospheric forcing and compare to the time series of current velocity and sea level anomalies. The vorticity index gives both the sign and magnitude of atmospheric vorticity; it was first proposed by Walsh et al. (1996) and then implemented by Dmitrenko et al. (2008a, 2008b) for describing atmospheric forcing over the Siberian shelves. The vorticity index is defined as the numerator of the finite difference Laplacian of SLP for an area within a radius of 550 km centered at 60°N and 85°W in Hudson Bay (**Figure 1**). A positive index corresponds to cyclonic atmospheric circulation that typically forces northerly winds over the mooring array in western Hudson Bay, whereas a negative vorticity index corresponds to anticyclonic atmospheric circulation that forces southerly winds over the mooring array. While the vorticity index used in this study does not fully explain the

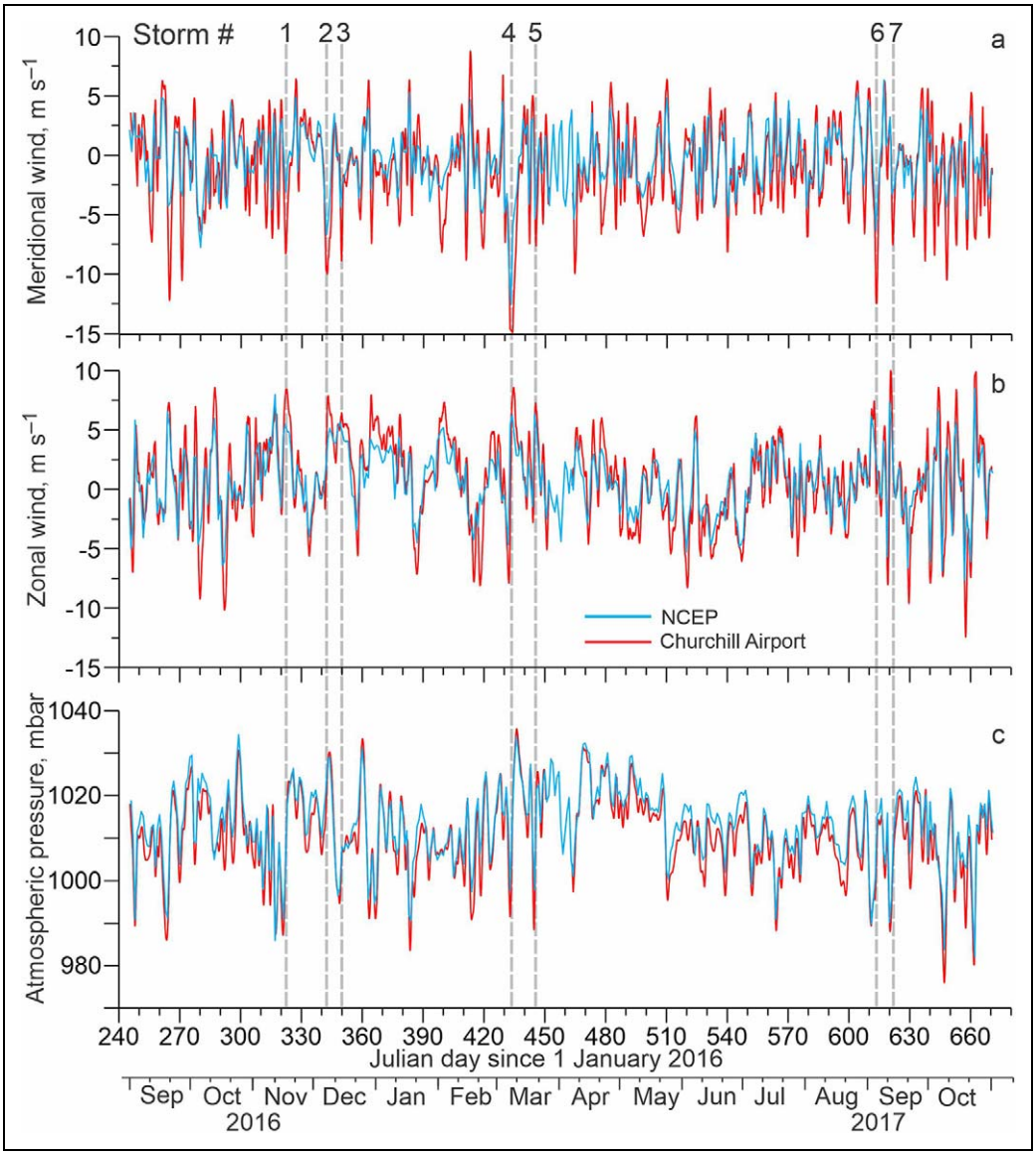

Figure 3. Time series of meridional and zonal winds and atmospheric pressure at Churchill. The 24-h mean (a) meridional, (b) zonal wind (m s^{-1}) and (c) atmospheric pressure (mbar) in Churchill retrieved from the airport weather station (red) and NCEP (blue). Vertical gray dashed lines identify storm events with northerly winds exceeding two standard deviations of the mean at AN01 with their reference numbers at the top. DOI: https://doi.org/10.1525/elementa.049.f3

observed variability of ocean circulation and SSH in western Hudson Bay (**Table 1**), it describes the intensity of cyclonic wind forcing over the entire Bay, which impacts the basin-scale circulation.

We examined the spatial uncertainty of atmospheric vorticity estimated at 60°N, 85°W by computing vorticity for the 5-point stencils with a central node shifted relative to 60°N, 85°W by approximately 280 km northward, eastward, southward, and westward (green, yellow, red, and black crosses and lines in **Figures 1** and **4**, respectively). **Figure 4** shows that vorticity computed at 60°N, 85°W (blue line in **Figure 4**) best describes major cyclonic storms observed during 2016–2017. We also conducted validity examination comparing the NCEP-derived vorticity to that computed using ERA5. For 2016–2017, the NCEP and ERA5-derived vorticities are coherent with a strong correlation of $k = 0.96$. The NCEP-derived vorticity slightly exceeds that obtained from ERA5 by $0.27 \pm 1.11\ s^{-1}$ (not shown), suggesting an insignificant difference between these two reanalyses.

The water dynamics and SSH on the bay-wide scale in Hudson Bay were assessed in a simulation of the Nucleus for European Modeling of the Ocean (NEMO) version 3.6 (Madec, 2008). We used the Arctic and the Northern Hemisphere Atlantic configuration, run at 1/4 degree. The model domain covers the Arctic and the Northern Hemisphere Atlantic with two open boundaries, one close to the Bering Strait in the Pacific Ocean and the other one at 20°S across the Atlantic Ocean. Open boundary conditions (temperature, salinity and horizontal ocean velocities) are derived from the monthly Global Ocean Reanalysis and Simulations produced by Mercator Ocean (Masina et al.,

Table 1. Correlations between atmospheric vorticity, along-shore wind, and sea level anomalies in western Hudson Bay for the full annual cycle and the ice-covered period.([a]/[b]) DOI: https://doi.org/10.1525/elementa.049.t1

		Along-shore wind		Sea level anomaly (SLA)			
Parameter	**Vorticity**	**AN01**	**NE03**	**Churchill**	**AN01**	**NE02**	**NE03**
Vorticity	–	–0.65/–0.72	–0.56/–0.65	0.49/0.41	0.14[c]/0.19[c]	0.57/0.62	0.54/0.58
Wind AN01	–0.65/–0.72	–	0.90/0.91	–0.40/–0.33	–0.21/–0.26	–0.62/–0.67	–0.60/–0.62
Wind NE03	–0.56/–0.65	0.90/0/91	–	–0.23/–0.22	–0.23/–0.27	–0.60/–0.63	–0.58/–0.61
SLA Churchill	0.49/0.41	–0.40/–0.33	–0.23/–0.22	–	0.70/0.64	0.57/0.61	0.63/0.62
SLA AN01	0.14[c]/0.19[c]	–0.21/–0.26	–0.23/–0.27	0.70/0.64	–	0.60/0.72	0.70/0.79
SLA NE02	0.57/0.62	–0.62/–0.67	–0.60/–0.63	0.57/0.61	0.60/0.72	–	0.94/0.99
SLA NE03	0.54/0.58	–0.60/–0.63	–0.58/–0.61	0.63/0.62	0.70/0.79	0.94/0.99	–

[a]Correlation computed for the entire period of observations: left value (before slash).

[b]Correlation computed only for the ice-covered period: right value (after slash).

[c]Correlation not statistically significant at the 99% confidence level.

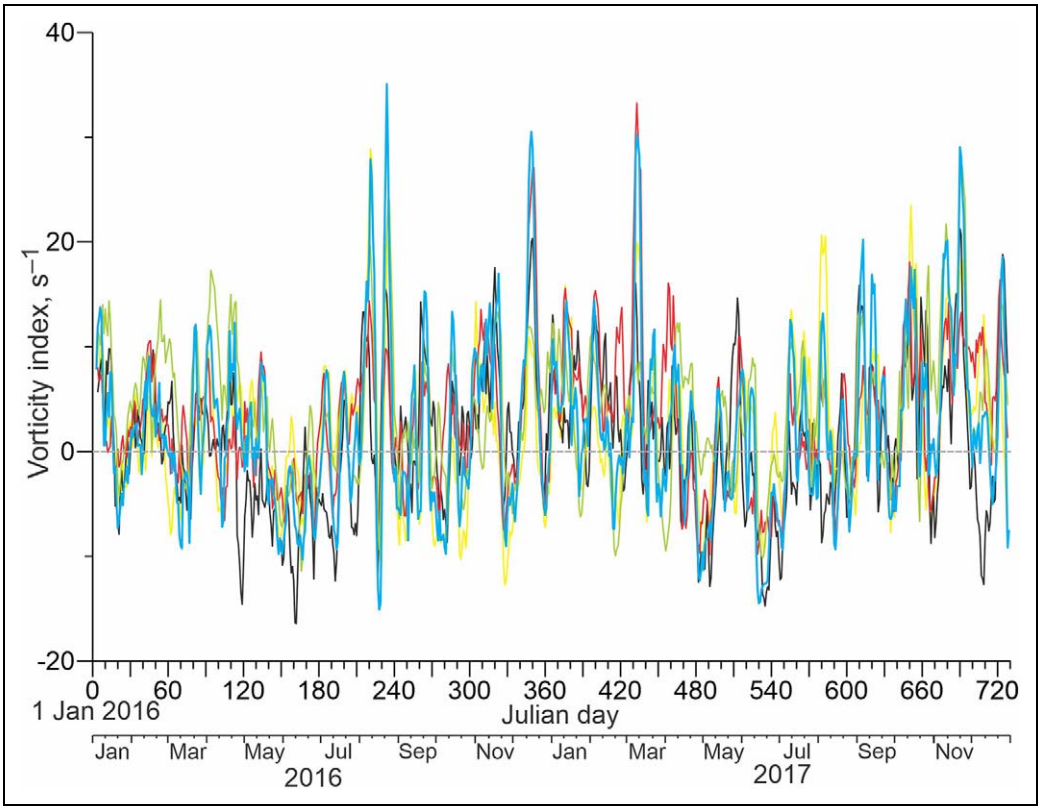

Figure 4. Vorticity time series for the Hudson Bay region. The 7-day running mean vorticity (s^{-1}) time series over Hudson Bay computed at 60°N, 85°W (blue line; Figure 1). Additional time series (black, green, yellow and red lines), derived from shifted nodes (green, yellow and red crosses in Figure 1), show the spatial uncertainty of atmospheric vorticity computed over Hudson Bay. DOI: https://doi.org/10.1525/elementa.049.f4

2017). The horizontal resolution over Hudson Bay is approximately 10–17 km. This model configuration consists of 50 vertical levels with enhanced resolution applied to the surface layer, providing a vertical resolution of less than 2 m for the layers in the top 10 m. Partial step was also enabled to better resolve the bathymetry. The simulation was integrated from 2002 to 2018, driven with atmospheric forcing data of high temporal (hourly) and spatial resolution (33 km) provided by the Canadian Meteorological Centre Global Deterministic Prediction System ReForecasts dataset (Smith et al., 2014b). Hudson Bay runoff came from the Hydrological Predictions for the Environment (Lindström et al., 2010; Andersson et al., 2013; Gelfan et al., 2017) model output which is discussed in

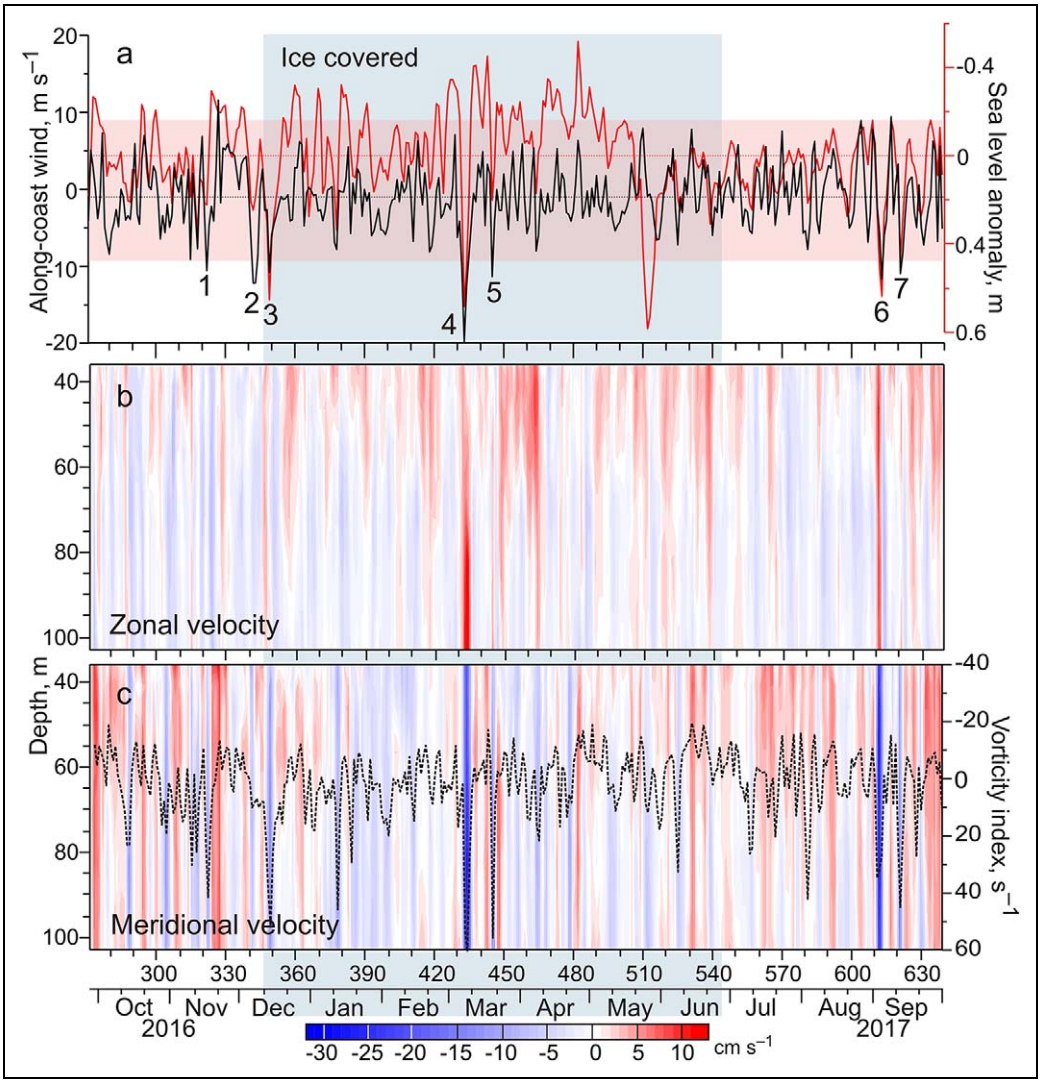

Figure 5. Time series of wind, sea level anomaly and current velocity for AN01. The (a) 24-h mean sea level anomaly (m) measured at the tide gauge in Churchill (red) and meridional 10-m wind velocity (black, m s^{-1}), and (b) zonal and (c) meridional current velocity (cm s^{-1}) as a function of depth for AN01. Blue shading highlights the ice-covered period following Kirillov et al. (2020). Pink shading (a) shows $\pm$ two standard deviations of the mean meridional wind velocity. Numbers identify storm events with northerly wind exceeding two standard deviations. Dashed black line (c) depicts vorticity index (s^{-1}), the finite-differenced numerator of the Laplacian of sea level atmospheric pressure computed for 60°N, 85°W. DOI: https://doi.org/10.1525/elementa.049.f5

more detail in Ridenour et al. (2019a). No salinity restoring was applied, in order to preserve the signal of freshwater from the runoff. Versions of this configuration have been extensively used and evaluated in the Labrador Sea (Feucher et al., 2019; Garcia-Quintana et al., 2019) and in the Canadian Arctic (Grivault et al., 2018; Hu et al., 2018). For studying the freshwater budget and seasonal circulation in Hudson Bay, Ridenour et al. (2019a, 2019b) showed that the model did a solid job of representing the main features of the Bay's hydrography and circulation. Meanwhile, Jafarikhasragh et al. (2019) showed that neither model resolution nor runoff had a major impact on the model's ability to simulate the sea surface temperature in Hudson Bay. Castro de la Guardia et al. (2019) showed the model well represented the seasonal sea-ice cycle in the Bay as part of a study on wind and sea-ice impacts on ocean productivity. Finally, Eastwood et al. (2020) used the model to examine winter circulation around the Belcher Islands in southeastern Hudson Bay.

Within this study, we used the hourly averaged model output to calculate the daily mean sea surface height and the zonal and meridional velocities during the 2016–2017 study period. The latter two were integrated horizontally and vertically with respect to their location on the model grid and in depth. Furthermore, the modelled volume outflow through Hudson Strait was calculated at top 30 m and compared to the atmospheric forcing.

Results

Year-long velocity data from western Hudson Bay, de-tided using an algorithm by Foreman (1977), showed moderate to slow circulation dominated by synoptic variability with periods lasting from a few days to about one week (**Figures 5b, c** and **6b, c**). At AN01, mean south-eastward

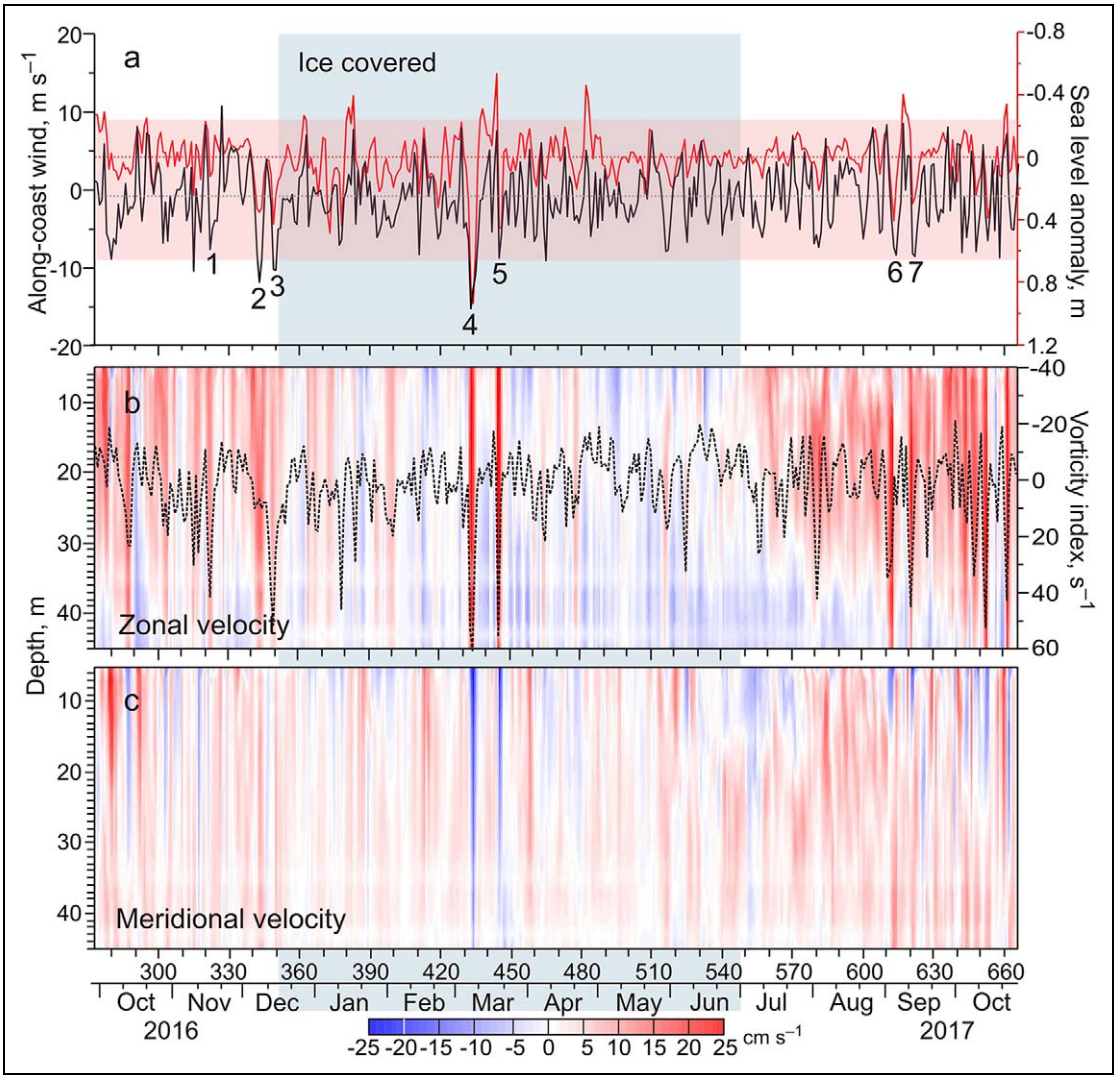

Figure 6. Time series of wind, sea level anomaly and current velocity for NE03. The (a) 24-h mean sea level anomaly (m) measured at NE02 (red), NCEP-derived meridional 10-m wind velocity (black, m s^{-1}), and (b) zonal and (c) meridional current velocity (cm s^{-1}) as a function of depth for NE03. Blue shading highlights the ice-covered period following Kirillov et al. (2020). Pink shading (a) shows $\pm$ two standard deviations of the mean meridional wind velocity. Numbers identify storm events with northerly wind at AN01 exceeding two standard deviations. Dashed black line (b) depicts vorticity index (s^{-1}), the finite-differenced numerator of the Laplacian of sea level atmospheric pressure computed for 60°N, 85°W. DOI: https://doi.org/10.1525/elementa.049.f6

velocity did not exceed 2 cm s^{-1} (blue line in **Figure 7a, b**), whereas at NE03 the mean velocity of $\sim$ 7 cm s^{-1} was more aligned to the east (blue line in **Figure 7c, d**). Velocity time series showed significant synoptic variability, which we attribute mainly to the near-barotropic southeastward flow events with speeds of up to 25 cm s^{-1} lasting 3–5 days (**Figures 5b, c** and **6b, c**). These events are characterized by southward meridional velocities at AN01 (blue shading in **Figure 5c**) and eastward zonal flow at NE03 (pink to red shading in **Figure 6b**). Moreover, the zonal velocity at NE03 shows seasonal variability with enhanced eastward transport during ice-free periods in October–December 2016 and July–October 2017 (**Figure 6b**).

We suggest that the synoptic variability of circulation in Hudson Bay, as observed by the mooring array, is governed by wind forcing. Hence, we examined the alongshore time series of daily-mean 10-m wind speeds for AN01 (meridional wind; **Figure 5a**) and NE01 (wind aligned to −11°T, where °T is the direction measured with reference to true north; **Figure 6a**). In the following, we focus on the northerly wind events, which enhance cyclonic water circulation in Hudson Bay. Based on the along-shore wind time series at AN01, we delineated seven storm events, during which northerly winds exceeded two standard deviations of the mean ($\pm$ 9 m s^{-1}; highlighted by pink shading in **Figure 5a**). Among these seven storms, #1 and #2 occurred during ice-free conditions in fall 2016, while storms #6 and #7 occurred during ice-free conditions in summer 2017. Storm #3 occurred during the onset of freeze-up (**Figures 5a and 6a**), while two consecutive events #4 and #5 occurred in March 2017 when the pack-ice thickness at AN01 and NE03 was $\sim$ 1.2 m (Kirillov et al., 2020). The strongest

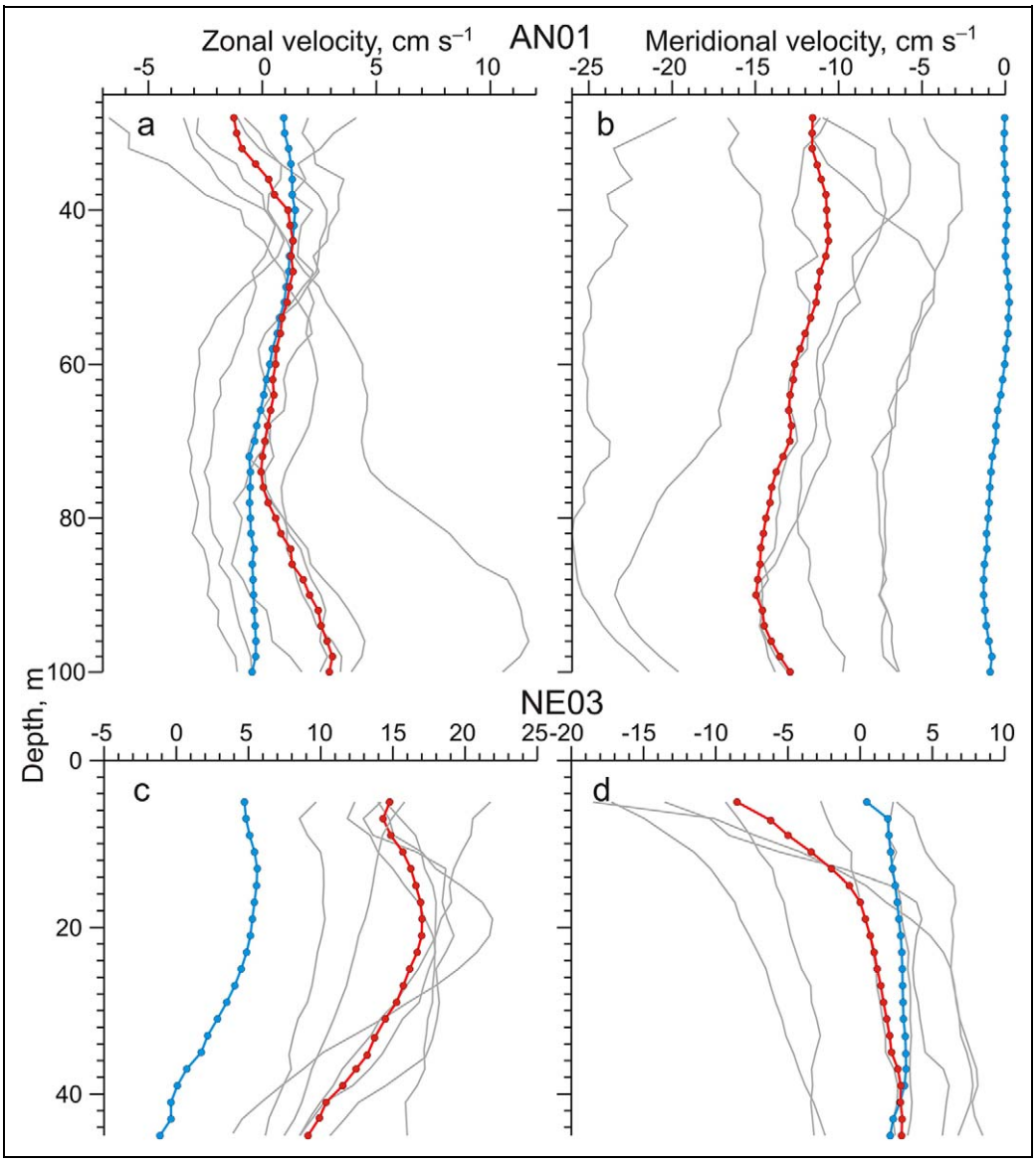

Figure 7. Vertical profiles of the zonal and meridional velocity for moorings AN01 and NE03. (a, c) Zonal and (b, d) meridional velocity (cm s^{-1}) for moorings (a, b) AN01 and (c, d) NE03. Blue line shows the year-mean. Red line depicts the mean for storms #1–7 with gray lines showing the mean for the individual storms. DOI: https://doi.org/10.1525/elementa.049.f7

northerly winds occurred during storm #4, reaching speeds of 20 m s^{-1} at AN01 (**Figure 5a**) and ∼ 16 m s^{-1} at NE03 (**Figure 6a**).

Velocity data show that pronounced northerly winds during these storms intensified ocean circulation in western Hudson Bay (**Figures 5** and **6**). More specifically, storms increased the southward velocity at AN01 to 5–26 cm s^{-1} with a mean of ∼ 13 cm s^{-1}, compared to an annual mean of just 2 cm s^{-1} (**Figures 5c** and **7b**; the mean was estimated over the time intervals of storms). The greatest increase in velocity was observed in response to storms #4 and #6 in March and September 2017, respectively (**Figure 5c** and **7b**). For NE03, however, storms increased the eastward flow to 10–22 cm s^{-1} with a mean of ∼ 14 cm s^{-1} (**Figures 6b** and **7c**), compared to an annual mean of ∼ 3.5 cm s^{-1} (**Figure 7c**). The increase in velocity was similar during all storms, except for storms #1 and #3 in November and December 2016, respectively (**Figure 6b**), when the eastward flow only increased by ∼ 7 cm s^{-1} (**Figure 7c**).

A statistically significant high correlation between the along-shore winds for AN01 and NE03 ($k = 0.90$, **Table 1**; this correlation and others presented later are statistically significant at the 99% confidence level) suggests that both mooring locations are impacted by the same atmospheric systems. The daily evolution of SLP patterns as the storms passed over Hudson Bay is presented for winter storm #4 (**Figure 8**) and summer storm #6 (**Figure 9**), with examples from the other storms provided as supplementary figures (Figures S1–S5). Six of the seven storms (#1 and #3–7) were the result of low pressure systems (cyclones) moving eastward over Hudson Bay toward Baffin Bay (storm #1; Figure S1a–d) or the Labrador Sea (storms #2–7; **Figures 8**, **9**, and S2–S5) with cyclone centres

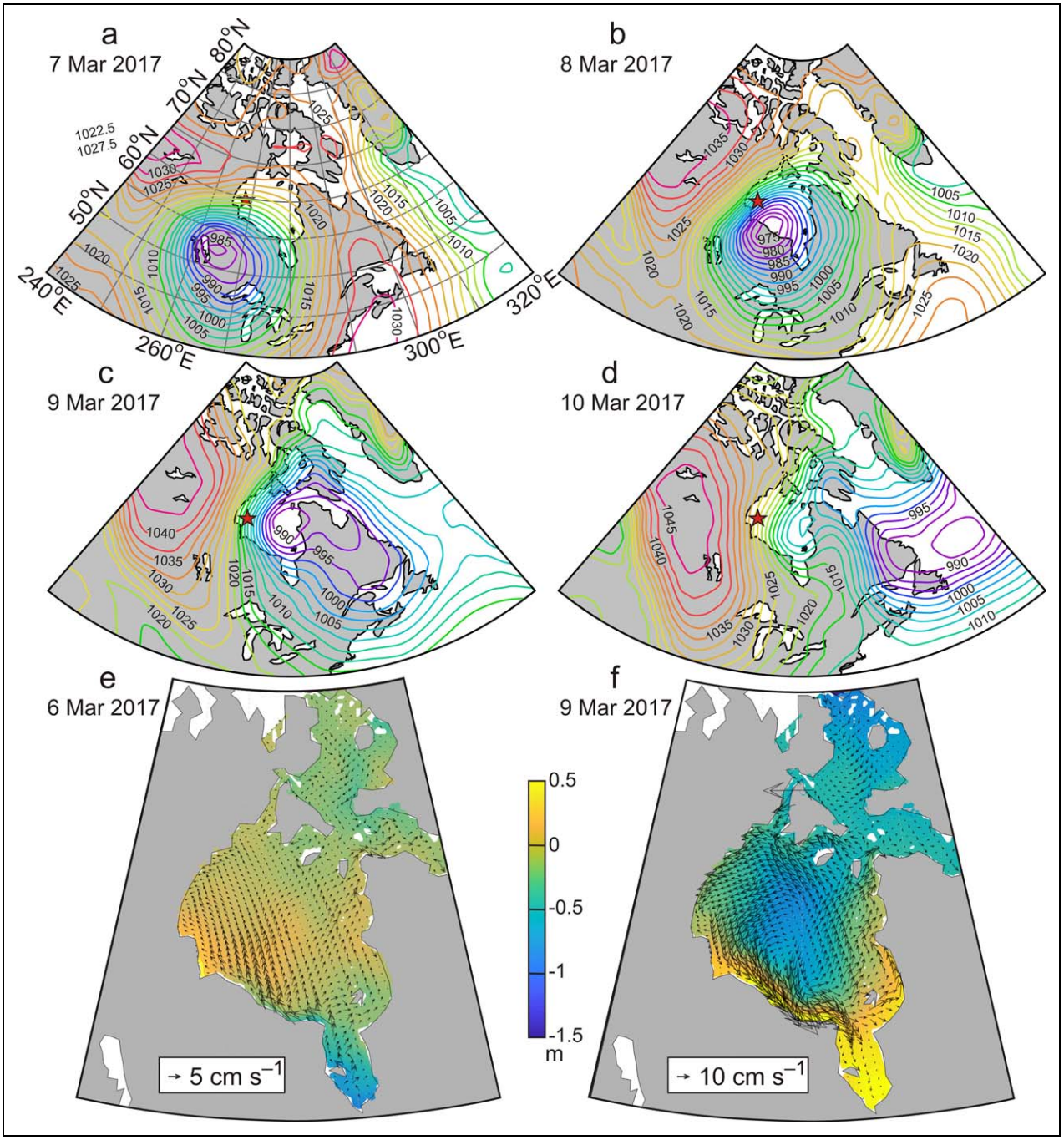

Figure 8. Sea level atmospheric pressure and simulated currents and sea surface heights for winter storm #4. (a–d) Sea level atmospheric pressure (hPa) for storm #4 (March 7–10, 2017) and simulated top 30-m currents (arrows) and SSH in color shading (e) before and (f) during the storm on 6 March and March 9, 2017, respectively. DOI: https://doi.org/10.1525/elementa.049.f8

passing directly over central Hudson and creating a tight SLP gradient of up to 0.02 hPa km^{-1} from central Hudson Bay to the coast. Alternatively, storm #2 was instead generated by high pressure to the west and a cyclone to the southeast of Hudson Bay, creating a tight SLP gradient across all of Hudson Bay (Figure S2).

Wind forcing over western Hudson Bay impacts sea level variability (**Figures 5a** and **6a**). Correlation between the along-shore wind velocities at AN01 and NE03 and sea level anomalies at Churchill and NE02 are –0.40 and –0.60, respectively (**Table 1**). These correlations suggest that northerly winds generate storm surge along western Hudson Bay. For example, during storms #3, #4, and #6, sea level at Churchill increased by ∼ 0.7 m (**Figure 5a**). However, the largest positive sea level anomaly at Churchill occurred from May 26 to 29, 2017 (∼ 0.8 m) and was not associated with wind forcing (**Figure 5a**), but instead related to flooding along the Churchill River. Moreover, this positive anomaly was not recorded in the Nelson River estuary at NE02 (**Figure 6a**).

An additional perspective on SSH response to atmospheric forcing over western Hudson Bay comes from

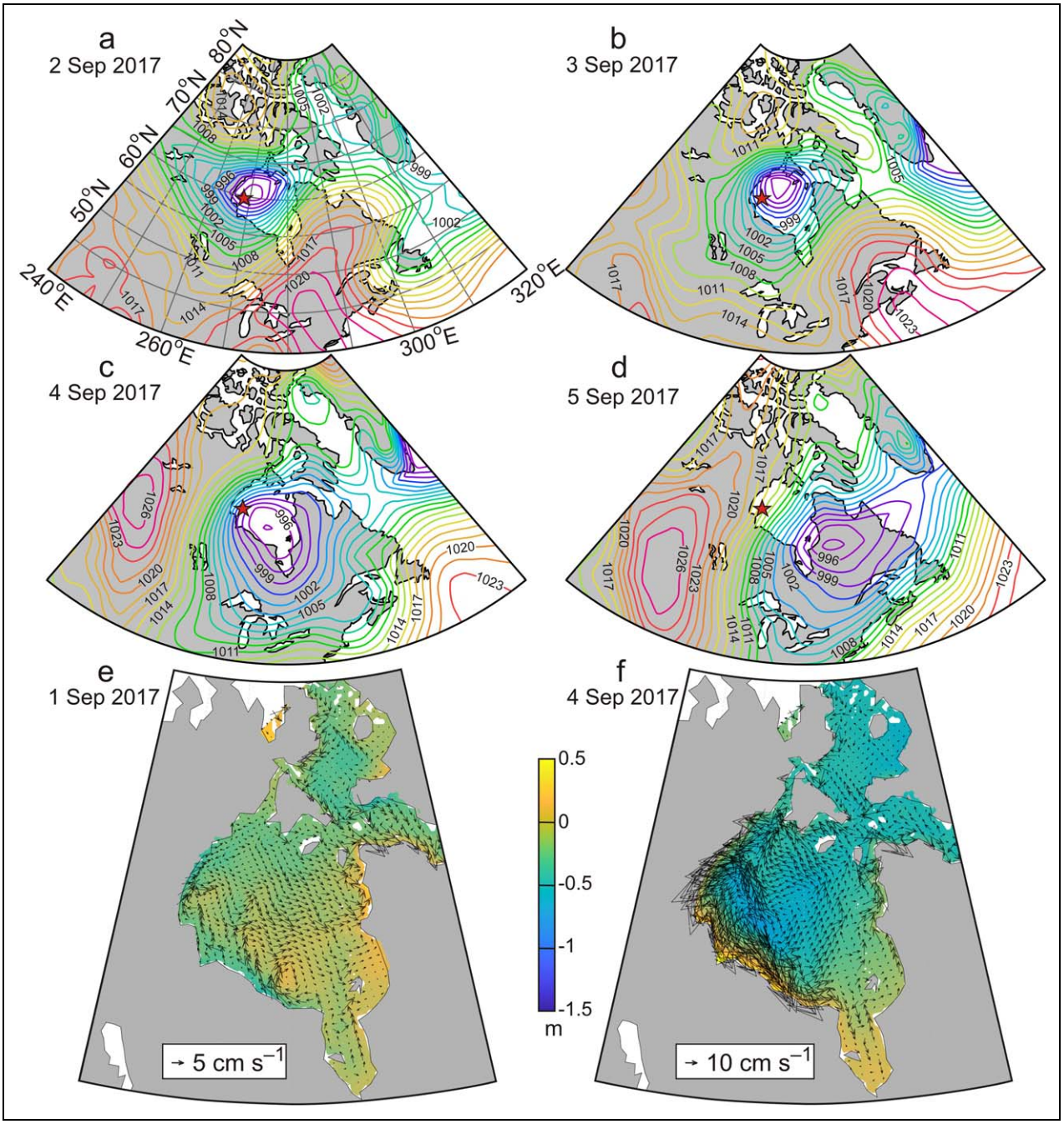

Figure 9. Sea level atmospheric pressure and simulated currents and sea surface heights for summer storm #6. (a–d) Sea level atmospheric pressure (hPa) for storm #6 (September 2–5, 2017) and simulated top 30 m currents (arrows) and SSH in color shading (e) before and (f) during the storm on September 1 and September 4, 2017, respectively. DOI: https://doi.org/10.1525/elementa.049.f9

a comparison of the off-shore wind time series with sea level anomaly at all bottom-anchored moorings (AN01 and NE02-03) and at Churchill (**Figure 10**). Analysis of the off-shore wind at AN01 and sea level at Churchill shows that northerly and northeasterly winds generate positive sea level anomalies of up to 0.4 m (**Figure 10c**). For AN01, located $\sim$ 180 km off-shore of Churchill, the sea level anomalies, attributed to wind forcing, were significantly less and did not exceed $\pm$ 0.1 m (**Figure 10d**). For the Nelson River estuary (NE02) and adjoining area (NE03), the SSH response to the off-shore wind forcing at NE03 was similar: northerly winds were generally associated with positive sea level anomalies (compare panels a and b in **Figure 10**). Furthermore, the largest positive sea level anomalies up to 0.4 m were generated in response to northwesterly winds. This wind direction is roughly consistent with the along–shore direction to the north of NE02/03 estimated as –11°T (**Figures 2** and **10b**). Overall, our data show that northerly winds in western Hudson Bay create storm surges along the coast.

In the following we use a vorticity index to characterize the effect of atmospheric forcing on: (1) SSH and (2) water

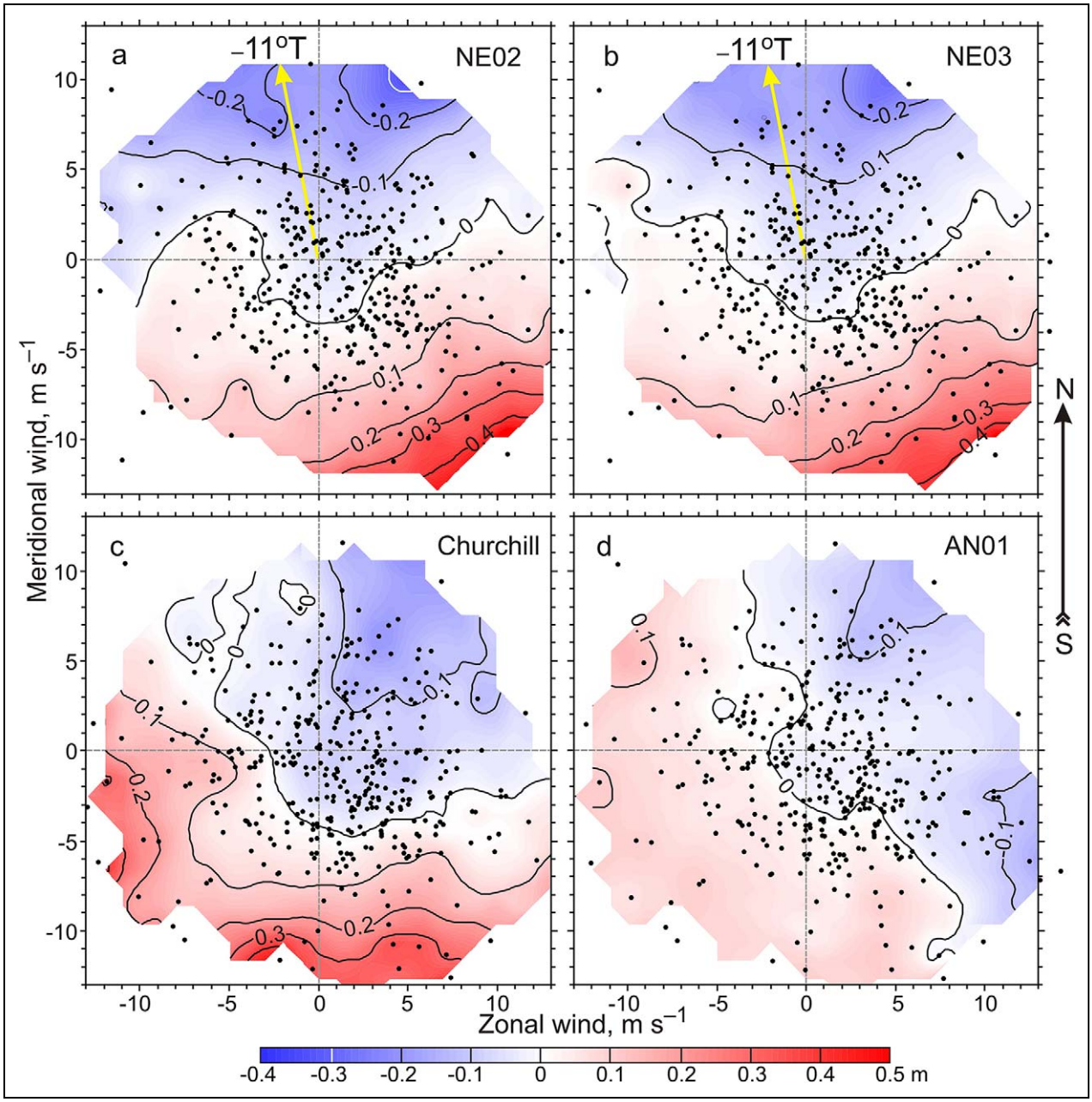

Figure 10. Sea level anomalies from the moored ADCPs and Churchill *versus* 10-m wind. Color shading shows daily mean sea level anomalies (m) from the moored ADCPs at (a) NE02, (b) NE03, (d) AN01, and (c) tide gauge in Churchill *versus* daily mean NCEP 10-m wind (m s^{-1}) at NE02 (top) and AN01 (bottom) from September 27, 2016 to October 27, 2017. Scatter plots show daily mean 10-m wind used for computing sea level anomalies. Blank areas represent insufficient data coverage. Yellow arrow (a, b) shows along-shore direction estimated as −11°T. DOI: https://doi.org/10.1525/elementa.049.f10

dynamics in western Hudson Bay. Correlation between the alongshore wind and vorticity for the entire year is –0.65 and –0.56 for AN01 and NE03, respectively (**Table 1**). During the ice-covered season, this correlation increased to –0.72 and –0.65, respectively (**Table 1**). The vorticity index correlates well with sea level at Churchill, NE02 and NE03 ($k = 0.49$, 0.57 and 0.54, respectively; **Table 1**). This correlation means that a cyclonic vorticity, associated with northerly winds over western Hudson Bay, generates a coastal storm surge. Positive sea level anomalies at Churchill, AN01, NE02 and NE03 are coherent with vorticity maxima observed during storms #1 and #3–7 (**Figure 11**). In contrast, the positive sea level anomaly that occurred during storm #2 is not attributable to enhanced cyclonic vorticity because of the different SLP pattern (Figure S2). Furthermore, there is no statistically significant correlation between sea level and vorticity for AN01, which was located ∼ 150 km from the coast (**Table 1**). Finally, a positive sea level anomaly at Churchill from 26 to May 29, 2017 is not associated with an enhanced atmospheric vorticity and was instead the result of flooding along the Churchill River. In summary, the

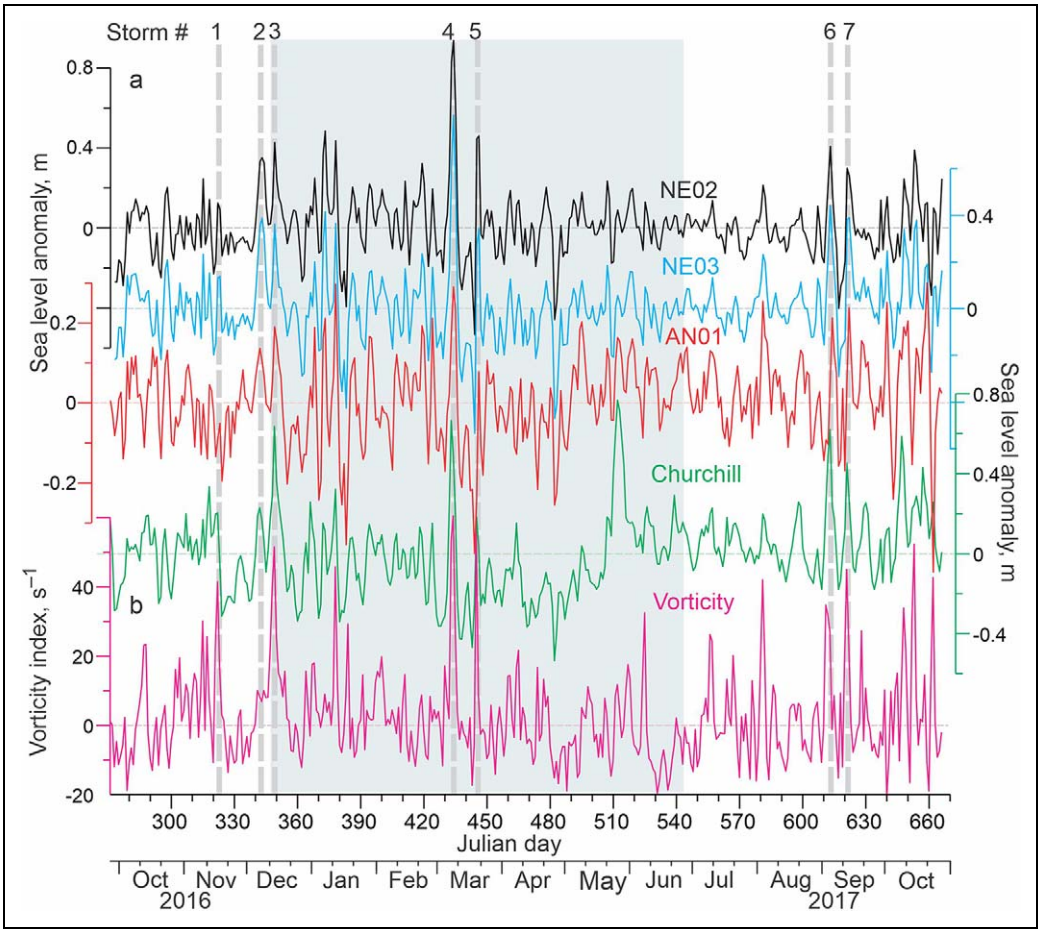

Figure 11. Time series of sea level anomalies at the moorings and Churchill, along with vorticity. Time series of the 24-h mean (a) sea level anomalies (m) measured at NE02 (black), NE03 (blue), AN01 (red) and the tide gauge in Churchill (green) and (b) vorticity index (s^{-1}). Gray dashed lines identify storm events with northerly wind exceeding two standard deviations of the mean at AN01 with their reference numbers at the top. Blue shading highlights the ice-covered period for AN01. DOI: https://doi.org/10.1525/elementa.049.f11

vorticity index represents cyclonic atmospheric forcing over Hudson Bay and explains ~ 25% of the variability in SSH in coastal areas of western Hudson Bay (Churchill, NE02 and NE03), but does not account for SSH variability in the off-shore area (AN01).

Finally, we examine the relationship between the daily-mean velocity at AN01 and NE03 and the daily-mean atmospheric vorticity. At AN01, the vorticity index correlates well with the meridional velocity over the entire water column. Correlation coefficients vary from –0.54 at 36-m depth to –0.64 at 82-m depth (not shown), suggesting a near-barotropic response of the meridional flow to wind forcing (**Figure 5c**). For example, at 45-m depth, correlation between the meridional velocity at AN01 and the vorticity index is –0.54 (**Figure 12a**). During the ice-covered period, correlation between the meridional velocity and vorticity index increases to –0.62 at 45-m depth (**Figure 12a**) and –0.63/–0.70 for 36/82-m depth (not shown). For all storm events except storm #2, peaks in vorticity coincide with enhanced southward flow (**Figure 12a**). In contrast to meridional velocity, the zonal velocity only correlates with vorticity in the bottom water layer (k = 0.25/0.46 for 82/100-m water depth, respectively; not shown). At NE03, the vorticity index correlates with the zonal velocity for the entire water column (**Figure 6b**), with the correlation gradually increasing with depth from 0.39 for the sub-surface water layer at 3-m depth (not shown) to 0.74 at the bottom water layer at 45-m depth (**Figure 12b**). For this depth level, all storm events except #2 generated enhanced eastward transport (**Figure 12b**). The meridional velocity at NE03 is also correlated with the vorticity index, though this correlation decays from k = –0.62 at 5-m depth to statistically insignificant values at > 3-m depth (not shown). Similar to AN01, the correlation between velocity at NE03 and vorticity is enhanced during the ice-covered period, increasing from 0.74 to 0.80 at 45-m depth (**Figure 12b**). At 20-m depth, this correlation increased from 0.55 to 0.74 (not shown).

A comparison of currents at AN01 and NE03 with atmospheric vorticity (**Figure 13**) provides an additional perspective on the response of currents to atmospheric forcing. At AN01, positive vorticity generates a south to southeastward flow approximately following the Hudson Bay shoreline (**Figures 1** and **13a, b**). In contrast, at NE03 positive vorticity forces a southeastward flow near the

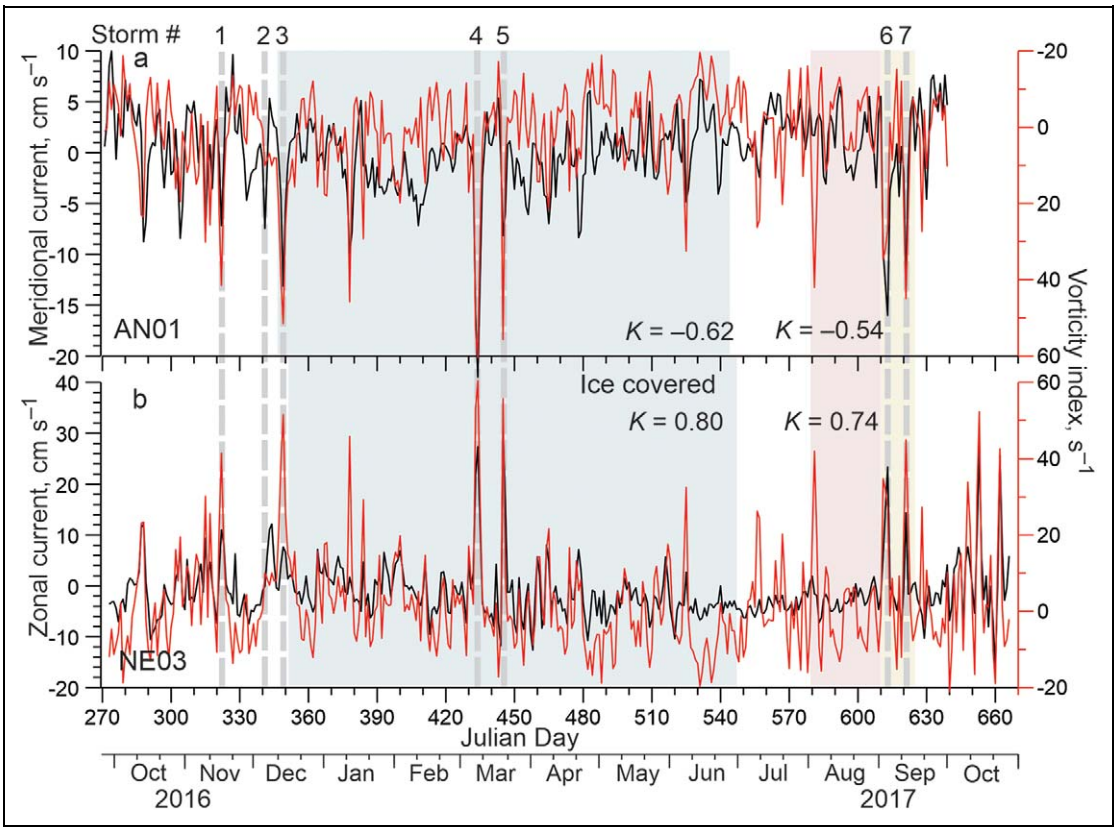

Figure 12. Time series of vorticity and current velocity at 45-m depth for AN01 and NE03. Time series of (a) meridional and (b) zonal currents (black, cm s^{-1}) at 45 m depth for AN01 and NE03, respectively. Vorticity index (s^{-1}) is depicted by the red line. Blue shading highlights the ice-covered period at each mooring. Gray dashed lines identify storm events with northerly wind exceeding two standard deviations of the mean at AN01 with their reference numbers at the top. Numbers show correlation (*K*) between currents and vorticity for the ice-covered period and for the entire time series. Pink and yellow shading highlight August and September 1–15, 2017 with predominant anticyclonic and cyclonic atmospheric forcing, respectively. (a) Vorticity axis is reversed for convenience. DOI: https://doi.org/10.1525/elementa.049.f12

surface (**Figure 13c**) and an eastward flow at depth (**Figure 13d**). At 45-m depth, the difference between AN01 and NE03 is obvious (compare panels a and d in **Figure 13**). Similar cyclonic atmospheric forcing generates mean southward water transport at AN01 (**Figure 12a**), while for NE03 the mean transport is eastward.

Discussion

Water dynamics in western Hudson Bay were found to be consistent with wind forcing. We suggest that an enhancement of the southeastward flow in western Hudson Bay is in line with patterns of atmospheric forcing generated by cyclones moving eastward over Hudson Bay. Cyclones passing over Hudson Bay (positive vorticity index in **Figures 4**, **5c**, **6b**, **11b** and **13**) generate northerly winds with a surface Ekman transport that moves waters onshore. The associated storm surges (**Figure 11a**) produce a pressure gradient normal to the coast that drives an alongshore southeastward geostrophic flow, similar to that described for the eastern Beaufort Sea by Dmitrenko et al. (2016, 2018).

The difference in water dynamics between AN01 and NE03 in response to similar atmospheric forcing (**Figures 5c, b**, **7b, c**, and **13a, d**) can be explained by the configuration of the coastline comprised by the Nelson River estuary (**Figures 1** and **2**). The storm surge along the southern coast of the Nelson River estuary in March 2017 in response to storms #4 and #5 resulted in a sea level anomaly of ~ 1 m (**Figure 14**). This sea level anomaly generated a cross-shelf pressure gradient that drove an alongshore eastward geostrophic flow recorded at NE03 (**Figure 6b**).

Our results show that the presence of sea ice increases momentum transfer from wind stress to the water column as the correlation between the vorticity index and currents increased during the ice-covered period (e.g., **Figure 12**). In particular, ice floes in a state of free drift within a partial or weak ice cover, typical of the polynya area in western Hudson Bay, increase the transfer of wind stress into the water column (Schulze and Pickart, 2012). An alternative explanation to the increased correlation during the ice-covered winter season may be that the linkage between the zonal wind forcing and atmospheric vorticity in western Hudson Bay is stronger due to a possible shift of cyclone trajectories during winter.

The vorticity index used in this study does not fully explain the observed variability of ocean circulation and SSH. In particular, the vorticity index did not capture the atmospheric forcing that drove pronounced northerly

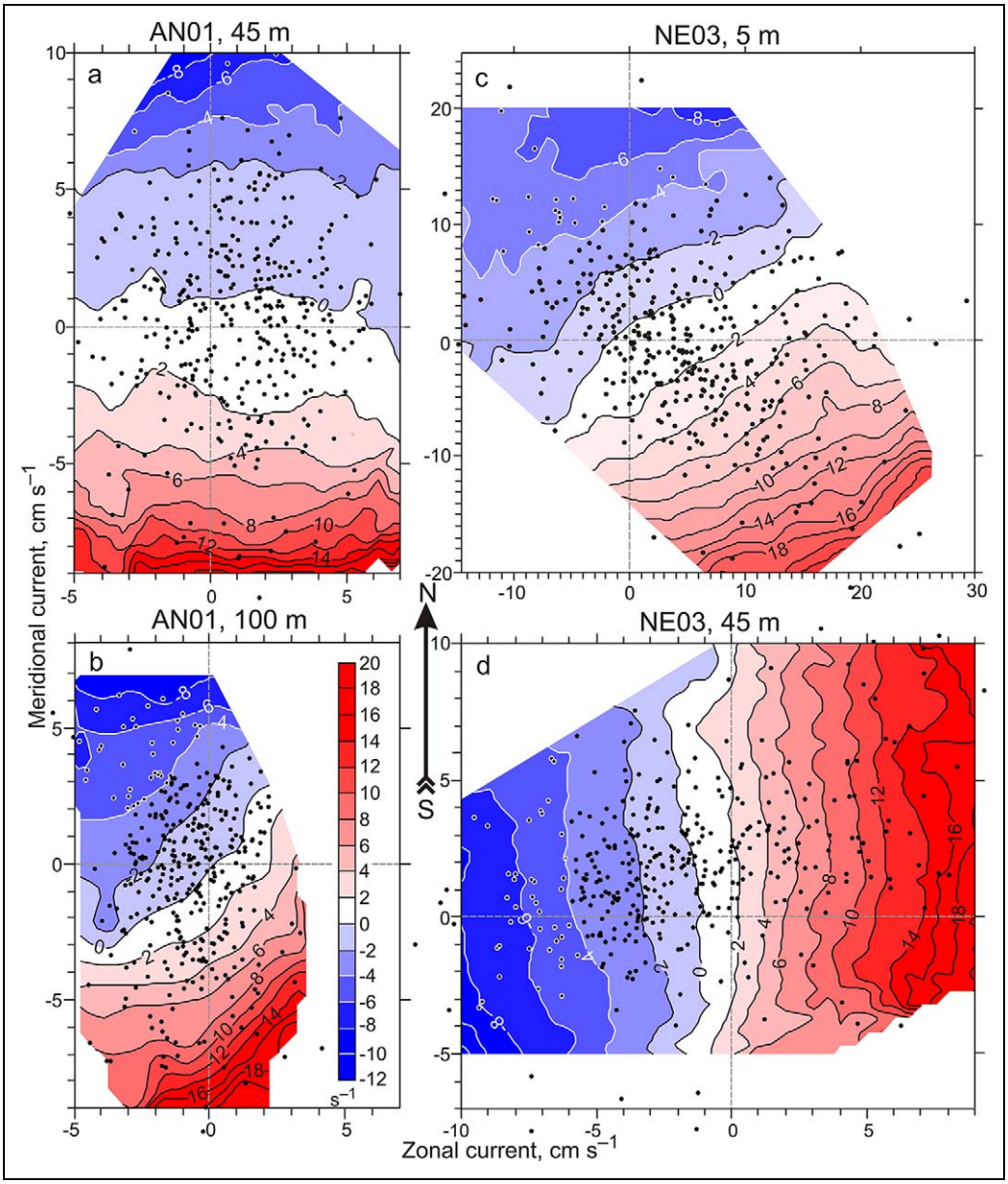

Figure 13. Atmospheric vorticity *versus* currents for AN01 and NE03. Color shading shows daily mean vorticity index (s^{-1}) *versus* currents (cm s^{-1}) for (left) AN01 at (a) 45-m depth and (b) 100-m depth, and (right) NE03 for (c) 5-m depth and (d) 45-m depth. Scatter plots show daily mean currents used for generating plots. Blank areas represent insufficient data coverage. DOI: https://doi.org/10.1525/elementa.049.f13

winds through western Hudson Bay during storm #2 (**Figure 11**). Storm #2, however, was not the result of a cyclone passing over Hudson Bay, but instead the result of high and low pressure systems passing on either side of the Bay and creating a bay-wide SLP gradient (Figure S2). Additionally, a localized peak in sea level at the Port of Churchill from 24 to May 28, 2017 did not correspond to positive vorticity because the increase in sea level was not the result of a cyclonically driven storm surge. Instead, the increase was due to flooding along the Churchill River as the spring freshet was dammed by ice at the mouth of the Churchill River. Water levels increased at Churchill during late May, peaking on 28 May. Observations carried out by Manitoba Hydro during this time showed ice near the river mouth was deteriorating and eventually opened up on 29 May, allowing river discharge to increase. Sea level at the port continued to drop while river discharge increased into June. This event shows that other factors beyond storm surges impact sea level at Churchill, though the vorticity index does explain 25% of the variability in sea level anomalies over the annual cycle (**Table 1**).

The process of cyclonic atmospheric forcing enhancing water circulation in western Hudson Bay can be applied to the entirety of Hudson Bay, as the spatial scales of cyclones during storms #1 and #3–7 roughly equal the Hudson Bay area (**Figures 8b**, **9b**, S1b, S3c, S4b and S5b). This scaling equivalency implies that cyclones passing over Hudson Bay cause on-shore Ekman transport and storm surges over the entire Hudson Bay coast as depicted schematically in **Figure 15a**. These effects produce a cross-

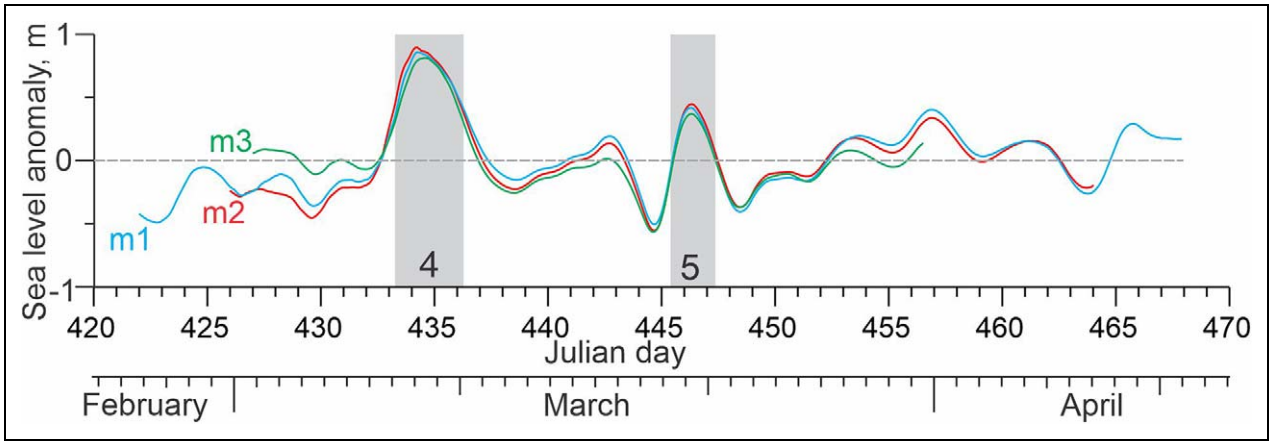

Figure 14. Sea level anomaly time series from the short-term moorings m1–m3. De-tided sea level anomaly time series (m) from the short-term moorings m1 (blue), m2 (red) and m3 (green) deployed from the landfast ice along the southern coast of the Nelson River estuary during February–April 2017 (see Figure 2 for mooring locations). Gray shading highlights storms #4 and #5 on 8–9 and March 20–21, 2017, respectively (for atmospheric forcing see Figures 8a–d and S4a–d, respectively). DOI: https://doi.org/10.1525/elementa.049.f14

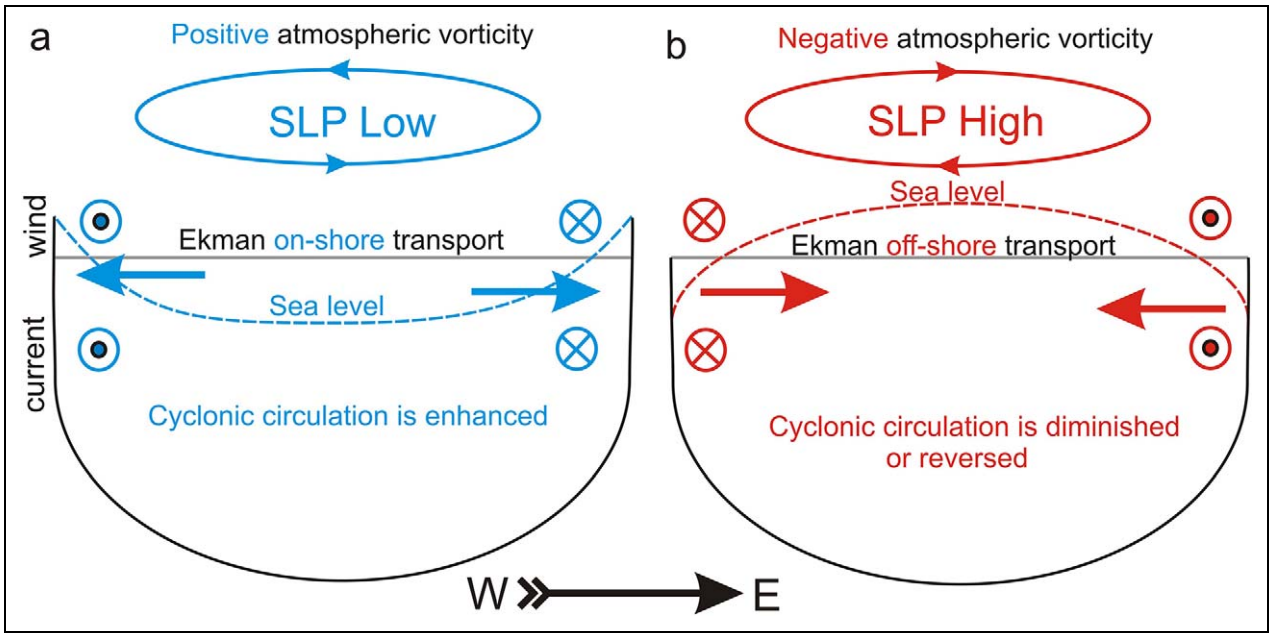

Figure 15. Diagram of the proposed impact of atmospheric vorticity on the Hudson Bay circulation. (a) Positive (cyclonic) vorticity causes onshore Ekman transport and storm surges over the coast, which produce a cross-slope pressure gradient that drives geostrophic flow favouring cyclonic circulation. (b) Negative (anticyclonic) vorticity forces off-shore Ekman transport, which produces a cross-slope pressure gradient, generating geostrophic flow in the opposite direction and diminishing or reversing cyclonic circulation. DOI: https://doi.org/10.1525/elementa.049.f15

shelf pressure gradient that drives alongshore geostrophic flow and favours the cyclonic circulation around Hudson Bay (**Figure 15a**). In contrast, a negative (anticyclonic) vorticity forces off-shore Ekman transport, which produces an opposite cross-slope pressure gradient and generates geostrophic flow in the opposite direction (**Figure 15b**). This flow diminishes or even reverses the Hudson Bay background thermohaline cyclonic circulation generated by coastal freshening.

Our interpretation of this process is further supported by bay-wide observations of sea surface height from satellite altimeters (**Figure 16**). Using two examples from summer 2017, we contrast the oceanic response during a period of cyclonic forcing from 1 to 15 September with a period of anticyclonic forcing during August. Storms #6 and 7 (yellow shading on **Figure 12**) made for cyclonic atmospheric circulation over Hudson Bay during early September 2017, with a positive mean vorticity index of 10.5 s^{-1}. In response to this forcing, positive SSH anomalies of 5–15 cm are observed throughout the coastal areas of Hudson Bay and negative SSH anomalies throughout central Hudson Bay (**Figure 16b**). In contrast, predominantly

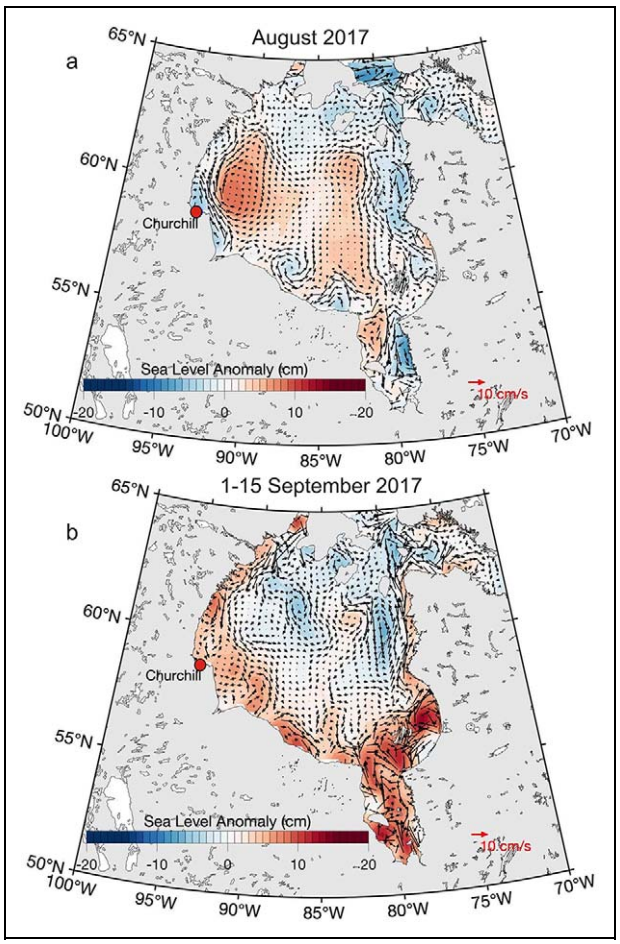

Figure 16. Sea surface height and geostrophic current anomalies for August and September 2017. Sea surface height (cm, color shading) and geostrophic current (arrows) anomalies relative to the 1993–2012 mean for (a) August 2017 and (b) September 1–15, 2017, highlighted in Figure 12 with pink and yellow shading, respectively. Sea surface height data derived from satellite altimeters. DOI: https://doi.org/10.1525/elementa.049.f16

anticyclonic forcing during August 2017 shows negative SSH anomalies in coastal areas and positive SSH anomalies of up to 8 cm in central Hudson Bay (**Figure 16a**). This pattern favours an opposite anticyclonic geostrophic circulation anomaly with velocities of 5–12 cm s^{-1} (**Figure 16a**).

The proposed interpretation of the mooring data is consistent with the results of model simulations conducted to extend our observations to the entire Hudson Bay (**Figures 8**, **9** and S1–S5, bottom panels). The response of SSH and upper 30-m velocities to storms #1 and #3–7 is in line with on-shore Ekman transport, a storm surge of up to 0.5 m along the Hudson Bay coast, and model along-shore currents of 20–25 cm s^{-1} comprising cyclonic circulation over the entire Hudson Bay (**Figures 8**, **9**, S1 and S3–S5). Cyclonic atmospheric forcing either enhances the Hudson Bay cyclonic circulation (storms #1, #3, #5 and #6; **Figures 9e, f**, S1e, f, S3e, f and S4e, f) or reverses anticyclonic circulation preceding the storms (storms #4 and #7; **Figures 8e, f** and S5e, f). The strongest cyclonic circulation was observed in response to storm #4 when the simulated velocities over western Hudson Bay exceeded 30 cm s^{-1} (**Figure 8f**), which is consistent with observations at AN01 (**Figure 5b, c**). Storm #2, however, did not strengthen cyclonic circulation around Hudson Bay (Figure S2e, f) because of the different atmospheric nature of this storm (Figure S2a–d). Overall, model simulations show enhancement of the Hudson Bay cyclonic circulation in response to the cyclonic atmospheric forcing, which, in turn, is well described by the vorticity index.

At first glance, our results supported an earlier hypothesis by Barber and Sydor (2014) that the wind patterns would directly impact the strength of the Hudson Bay boundary current and stronger cyclonic/anticyclonic atmospheric forcing would favour a larger export/storage of freshwater in Hudson Bay. To test this hypothesis, we computed the volume transport through Hudson Strait during 2016–2017 from the NEMO model output (**Figure 17**). The volume transport is subject to seasonality with enhanced outflow from November 2016 into January 2017 and from mid-September through December 2017, when the mean atmospheric vorticity was elevated up to 5.6 s^{-1} and 2.7 s^{-1}, respectively (**Figure 17**). However, the time series of atmospheric vorticity and volume flux are poorly correlated and there is no evidence that storms #1 and #4–7 increased the outflow through Hudson Strait (**Figure 17**). These results suggest that atmospheric vorticity alone cannot explain freshwater outflow through Hudson Strait, and that the trajectories of individual cyclones can be important.

Finally, the model simulation confirms the difference in the direction of currents observed at AN01 and NE03 (e.g., **Figure 13a, d**). For example, over the area adjoining the Nelson River estuary, currents during storms #2, 3, 5, 6 and 7 tended to turn eastward (**Figures 7f**, S2f, S3f, S4f and S5f). In contrast, currents were mainly directed southward for the AN01 area.

Conclusions

We analyzed the year-long time series of currents from two oceanographic moorings deployed along the western coast of Hudson Bay from September 2016 to September/October 2017 under the framework of Hudson Bay System (BaySys) Study to examine atmospheric controls on water circulation in Hudson Bay. Our analysis revealed relationships between wind forcing, atmospheric vorticity, sea level variability and currents. We found that the along-shore southeastward current is amplified in western Hudson Bay in response to northerly winds associated with cyclones passing over Hudson Bay. We used an atmospheric vorticity index derived from NCEP SLP to characterize the wind forcing and to compare vorticity with ocean current velocities and sea level time series. Our analysis revealed that along the western coast of Hudson Bay, atmospheric vorticity correlates with sea level and along-shore currents. Our interpretation is that a surface Ekman on-shore transport and associated increase of sea level over the coastal area produce a cross-slope pressure gradient. This gradient drives an along-shore

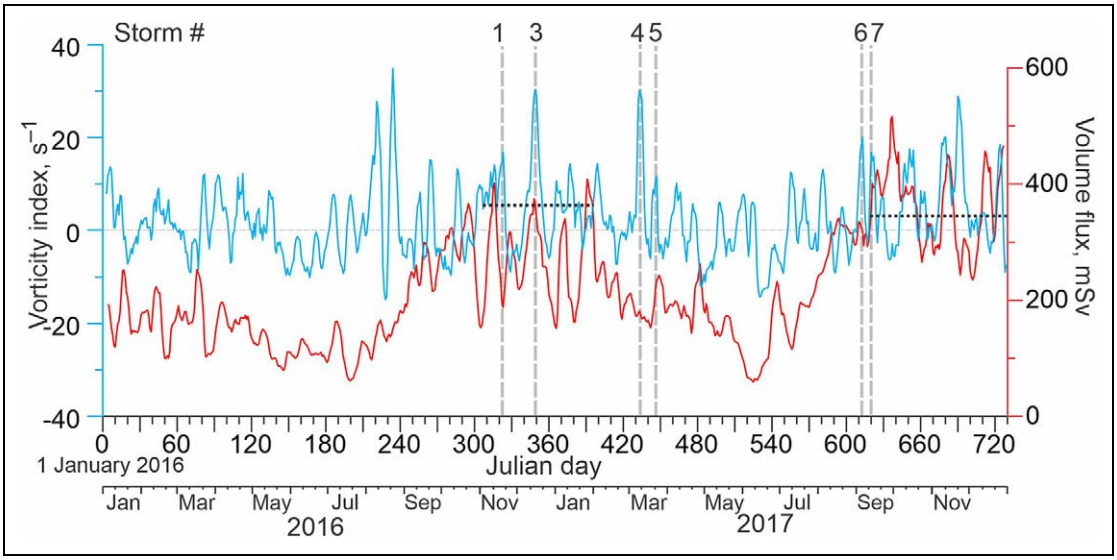

Figure 17. Atmospheric vorticity and volume outflow at Hudson Strait. The 7-day running mean of atmospheric vorticity over Hudson Bay (blue, s^{-1}) and simulated top 30-m volume outflow at Hudson Strait (red, mSv). Horizontal black dashed lines show mean vorticity for November 2016 to January 2017 and mid-September to December 2017. DOI: https://doi.org/10.1525/elementa.049.f17

southeastward flow, in the same direction as the wind. The wind-driven circulation is consistent with (1) sea level patterns provided by both satellite altimetry observations and model simulations and (2) simulated ocean currents. They allowed us to extend our conclusions to the bay-wide scale and show that cyclonic forcing enhances the alongshore transport of riverine water around Hudson Bay.

Based on the results presented in this paper, wind forcing can balance or favor the estuarine thermohaline forcing. A cyclonic wind forcing is suggested to drive an enhanced cyclonic water circulation over the entire Hudson Bay (**Figure 15a**). Thus, recurring cyclonic wind forcing favors freshwater transport along the Hudson Bay coastline towards Hudson Strait. As a result, a significant reduction in the residence time of riverine water in Hudson Bay can be expected, with important implications for water column stability and thus primary production and support of the Hudson Bay ecosystem (e.g., Barbedos de Freitas et al., 2020; Pierrejean et al., 2020). During an anticyclonic wind forcing, the background thermohaline cyclonic circulation in Hudson Bay is expected to slow down or even reverse (**Figure 15b**). This effect would likely result in a reduction of the freshwater transport to Hudson Strait and an increase of the riverine water residence time in the bay.

Our results, however, show no direct relationship between cyclonic storms over the bay and volume outflow through Hudson Strait "(**Figure 17**), suggesting an integrative response to cyclonic forcing rather than a direct impact". The time frame of our analysis does not allow us to quantify freshwater export and storage, clearly defining the need for further research in this area using multi-year numerical simulations and atmospheric reanalyses. Further research is also needed to investigate how thermohaline circulation responds to wind and buoyancy forcing. The seasonality of atmospheric forcing and its climatic aspects are also important priorities for future research.

Data accessibility statement

The ADCP data used in research are available through the Polar Data Catalogue at https://www.polardata.ca (CCIN Reference 13105). The NEMO model is available through the NEMO website (http://www.nemoocean.eu/). The ANHA configuration and its output can be accessed through Compute Canada (www.computecanada.ca).

Supplemental material

The supplemental files for this article can be found as follows:

Figures S1–S5. Docx

Figure S1. Sea level atmospheric pressure and simulated currents and sea surface heights for storm #1. (a–d) Sea level atmospheric pressure (hPa) for storm #1 (16–19 November 2016) and simulated top 30-m currents (arrows) and SSH in color shading (e) before and (f) during the storm on November 16 and 18, 2016, respectively (JPEG).

Figure S2. Sea level atmospheric pressure and simulated currents and sea surface heights for storm #2. (a–d) Sea level atmospheric pressure (hPa) for storm #2 (December 7–10, 2016) and simulated top 30-m currents (arrows) and SSH in color shading (e) before and (f) during the storm on December 7 and 9, 2016, respectively (JPEG).

Figure S3. Sea level atmospheric pressure and simulated currents and sea surface heights for storm #3. (a–d) Sea level atmospheric pressure (hPa) for storm #3 (December 12–15, 2016) and simulated top 30-m currents (arrows) and SSH in color shading (e) before and (f) during the storm on December 12 and 15, 2016, respectively (JPEG).

Figure S4. Sea level atmospheric pressure and simulated currents and sea surface heights for storm #5. (a–d) Sea level atmospheric pressure (hPa) for storm #5 (March 19–22, 2017) and simulated top 30-m currents (arrows)

and SSH in color shading (e) before and (f) during the storm on March 19 and 21, 2017, respectively (JPEG).

Figure S5. Sea level atmospheric pressure and simulated currents and sea surface heights for storm #7. (a–d) Sea level atmospheric pressure (hPa) for storm #7 (September 11–14, 2017) and simulated top 30-m currents (arrows) and SSH in color shading (e) before and (f) during the storm on September 10 and 13, 2017, respectively (JPEG).

Acknowledgments

This work is a contribution to the Arctic Science Partnership (ASP) and ArcticNet. The model experiment was performed on Compute Canada infrastructure.

Funding

The author(s) disclosed receipt of the following financial support for the research, authorship, and/or publication of this article: This work is a contribution to the Natural Sciences and Engineering Council of Canada (NSERC) Collaborative Research and Development project: BaySys (CRDPJ470028-14). Funding for this work, including field studies, was provided by NSERC, Manitoba Hydro, the Canada Excellence Research Chair (CERC) program, the Canada Research Chairs (CRC) program, and the base funds of NOAA Atlantic Oceanographic and Meteorological Laboratory. DLV was supported by the NASA Ocean Surface Topography Science Team program (via the grant NNX17AH59G) and by the NOAA Atlantic Oceanographic and Meteorological Laboratory under the auspices of the Cooperative Institute of Marine and Atmospheric Studies (CIMAS) of the University of Miami and NOAA, Cooperative Agreement NA10OAR4320143. D Babb is additionally supported by NSERC and the Canadian Meteorological and Oceanographic Society (CMOS).

Competing interests

The authors have no competing interests to declare.

Author contributions

Contributed to conception and design: IAD, PGM, DGBarber.

Contributed to acquisition of data: IAD, DLV, SAK, DGBabb, JKE.

Contributed to analysis and interpretation of data: IAD, PGM, DLV, RT, KS, JVL.

Drafted and/or revised the article: IAD, PGM, DLV, SAK, KS, JKE, DGBabb.

Approved the submitted version for publication: IAD.

References

Andersson, JCM, Pechlivanidis, IG, Gustafsson, D, Donnelly, C, Arheimer, B. 2013. Key factors for improving large-scale hydrological model performance, in Lekkas, T. ed., *Proceedings of the 13th international conference on environmental science and technology*, Athens, Greece. Sep 05–07, 2013, pp. 77–88.

Bamber, JL, Tedstone, AJ, King, MD, Howat, IM, Enderlin, EM, van den Broeke, MR, Noel, B. 2018. Land ice freshwater budget of the Arctic and North Atlantic Oceans: 1. Data, methods, and results. *J Geophys Res Oceans* **123**: 1827–1837. DOI: http://dx.doi.org/10.1002/2017JC013605.

Barbados de Freitas, L, Bélanger, S, Tremblay, J-É. 2020. Climate control of sea-ice-edge phytoplankton blooms in the Hudson Bay System. *Elem Sci Anth*, in press.

Barber, D, Sydor, K. 2014. Freshwater-marine coupling in the Hudson Bay IRIS, in *ArcticNet annual research compendiums (2013–2014), marine systems*. Québec, Canada: Univ Laval: 12. Available at https://arcticnet.ulaval.ca//pdf/phase3/freshwater-marine-coupling.pdf.

Castro de la Guardia, L, Garcia-Quintana, Y, Claret, M, Hu, X, Galbraith, ED, Myers, PG. 2019. Assessing the role of high-frequency winds and sea ice loss on Arctic phytoplankton blooms in an ice-ocean-biogeochemical model. *J Geophys Res: Biogeosciences* **124**: 2728–2750. DOI: http://dx.doi.org/10.1029/2018JG004869.

Copernicus Climate Change Service (C3S). 2017. ERA5: Fifth generation of ECMWF atmospheric reanalyses of the global climate. Copernicus Climate Change Service Climate Data Store (CDS). Last accessed on November 5, 2020.

Dee, DP, Uppala, SM, Simmons, AJ, Berrisford, P, Poli, P, Kobayashi, S, Andrae, U, Balmaseda, MA, Balsamo, G, Bauer, P, Bechtold, P, Beljaars, ACM, van de Berg, L, Bidlot, J, Bormann, N, Delsol, C, Dragani, R, Fuentes, M, Geer, AJ, Haimberger, L, Healy, SB, Hersbach, H, Hólm, EV, Isaksen, L, Kållberg, P, Köhler, M, Matricardi, M, McNally, AP, Monge-Sanz, BM, Morcrette, J-J, Park, B-K, Peubey, C, de Rosnay, P, Tavolato, C, Thépaut, J-N, Vitart, F. 2011. The ERA-interim reanalysis: Configuration and performance of the data assimilation system, *Q J R Meteorol Soc* **137**(656): 553–597. DOI: http://dx.doi.org/10.1002/qj.828.

Déry, SJ, Mlynowski, TJ, Hernández-Henríquez, MA, Straneo, F. 2011. Interannual variability and interdecadal trends in Hudson Bay streamflow. *J Mar Syst* **88**(3): 341–351. DOI: http://dx.doi.org/10.1016/j.jmarsys.2010.12.002.

Déry, SJ, Stieglitz, M, McKenna, EC, Wood, EF. 2005. Characteristics and trends of river discharge into Hudson, James, and Ungava Bays, 1964–2000. *J Climate* **18**: 2540–2557. DOI: http://dx.doi.org/10.1175/JCLI3440.1.

Dmitrenko, IA, Kirillov, SA, Forest, A, Gratton, Y, Volkov, DL, Williams, WJ, Lukovich, JV, Belanger, C, Barber, DG. 2016. Shelfbreak current over the Canadian Beaufort Sea continental slope: Wind-driven events in January 2005. *J Geophys Res Oceans* **121**: 2447–2468. DOI: http://dx.doi.org/10.1002/2015JC011514.

Dmitrenko, IA, Kirillov, SA, Myers, PG, Forest, A, Tremblay, B, Lukovich, JV, Gratton, Y, Rysgaard, S, Barber, DG. 2018. Wind-forced depth-dependent currents over the eastern Beaufort Sea continental

slope: Implications for Pacific water transport. *Elem Sci Anth* **6**: 66. DOI: http://dx.doi.org/10.1525/elementa.321.

Dmitrenko, IA, Kirillov, SA, Tremblay, LB. 2008a. The long-term and interannual variability of summer fresh water storage over the eastern Siberian shelf: Implication for climatic change. *J Geophys Res* **113**: C03007. DOI: http://dx.doi.org/10.1029/2007JC004304.

Dmitrenko, IA, Kirillov, SA, Tremblay, LB, Bauch, D, Makhotin, M. 2008b. Effects of atmospheric vorticity on the seasonal hydrographic cycle over the eastern Siberian shelf, *Geophys Res Lett* **35**: L03619. DOI: http://dx.doi.org/10.1029/2007GL032739.

Eastwood, RA, McDonald, R, Ehn, J, Heath, J, Arragutainaq, L, Myers, PG, Barber, D, Kuzyk, ZZ. 2020. Role of river runoff and sea-ice brine rejection in controlling stratification throughout winter in southeast Hudson Bay. *Estuaries and Coasts* **43**: 756–786. DOI: http://dx.doi.org/10.1007/s12237-020-00698-0.

Feucher, CE, Garcia-Quintana, Y, Yashayaev, I, Hu, X, Myers, PG. 2019. Labrador Sea Water formation rate and its impact on the local Meridional Overturning Circulation. *J Geophys Res: Oceans* **124**: 5654–5670. DOI: http://dx.doi.org/10.1029/2019JC015065.

Foreman, MGG. 1977. Manual for tidal heights analysis and prediction. *Pacific Marine Science Report*, 77–10, Patricia Bay, Sidney, BC: Institute of Ocean Sciences, 58 pp.

Garcia-Quintana, Y, Courtois, P, Hu, X, Pennelly, C, Kieke, D, Myers, PG. 2019. Sensitivity of Labrador Sea Water formation to changes in model resolution, atmospheric forcing, and freshwater input. *J Geophys Res: Oceans* **124**: 2126–2152. DOI: http://dx.doi.org/10.1029/2018JC014459.

Gelfan, A, Gustafsson, D, Motovilov, Y, Arheimer, B, Kalugin, A, Krylenko, I, Lavrenov, A. 2017. Climate change impact on the water regime of two great Arctic rivers: Modeling and uncertainty issues. *Clim Change* **141**: 499–515. DOI: http://dx.doi.org/10.1007/s10584-016-1710-5.

Granskog, MA, Macdonald, RW, Kuzyk, ZA, Senneville, S, Mundy, C-J, Barber, DG, Stern, GA, Saucier, F. 2009. Coastal conduit in southwestern Hudson Bay (Canada) in summer: Rapid transit of freshwater and significant loss of colored dissolved organic matter. *J Geophys Res* **114**: C08012. DOI: http://dx.doi.org/10.1029/2009JC005270.

Grivault, N, Hu, X, Myers, PG. 2018. Impact of the surface stress on the volume and freshwater transport through the Canadian Arctic Archipelago from a high-resolution numerical simulation. *J Geophys Res: Oceans* **123**: 9038–9060. DOI: http://dx.doi.org/10.1029/2018JC013984.

Hachey, HB. 1935. The circulation of Hudson Bay Water as indicated by drift bottles. *Science New Series* **82**(2125): 275–276.

Hochheim, KP, Barber, DG. 2011. Atmospheric forcing of sea ice in Hudson Bay during the fall period, 1980–2005. *J Geophys Res* **115**: C05009. DOI: http://dx.doi.org/10.1029/2009JC005334.

Hochheim, KP, Barber, DG. 2014. An update on the ice climatology of the Hudson Bay System. *Arctic Antarctic Alpine Res* **46**(1): 66–83. DOI: http://dx.doi.org/10.1657/ 1938-4246-46.1.66.

Hoffmann, L, Gebhard, G, Li, D, Stein, O, Wu, X, Griessbach, S, Heng, Y, Konopka, P, Müller, R, Vogel, B, Wright, JS. 2019. From ERA-Interim to ERA5: The considerable impact of ECMWF's next-generation reanalysis on Lagrangian transport simulations. *Atmos Chem Phys* **19**: 3097–3124. DOI: http://dx.doi.org/10.5194/acp-19-3097-2019.

Hu, X, Sun, J, Chan, TO, Myers, PG. 2018. Thermodynamic and dynamic ice thickness contributions in the Canadian Arctic Archipelago in NEMO-LIM2 numerical simulations. *Cryosphere* **12**: 1233–1247. DOI: http://dx.doi.org/10.5194/tc-12-1233-2018.

Ingram, RG, Prinsenberg, S. 1998. Coastal oceanography of Hudson Bay and surrounding Eastern Canadian Arctic Waters, in **Robinson, AR, Brink, KN** eds., *The sea*, Vol. 11. *The global coastal ocean regional studies and synthesis*. Harvard University Press, Cambridge, Massachusetts and London: 835–861.

Jafarikhasragh, S, Lukovich, JV, Hu, X, Myers, PG, Sydor, K, Barber, DG. 2019. Modelling sea surface temperature (SST) in the Hudson Bay Complex using bulk heat flux parameterization: Sensitivity to atmospheric forcing, and model resolution. *Atmos-Ocean* **57**(2): 120–133. DOI: http://dx.doi.org/10.1080/07055900.2019.1605974.

Jones, EP, Anderson, LG. 1994. Northern Hudson Bay and Foxe Basin: Water masses, circulation and productivity. *Atmos-Ocean* **32**(2): 361–374. DOI: http://dx.doi.org/10.1080/07055900.1994.9649502.

Kalnay, E, Kanamitsu, M, Kistler, R, Collins, W, Deaven, D, Gandin, L, Iredell, M, Saha, S, White, G, Woollen, J, Zhu, Y, Chelliah, M, Ebisuzaki, W, Higgins, W, Janowiak, J, Mo, KC, Ropelewski, C, Wang, J, Leetmaa, A, Reynolds, R, Jenne, R, Joseph, D. 1996. The NCEP/NCAR 40-year reanalysis project. *Bull Am Meteorol Soc* **77**: 437–471. DOI: http://dx.doi.org/10.1175/1520-0477(1996)077<0437: TNYRP>2.0.CO;2.

Kirillov, S, Babb, D, Dmitrenko, I, Landy, J, Lukovich, J, Ehn, J, Sydor, K, Barber, D, Stroeve, J. 2020. Atmospheric forcing drives the winter sea ice thickness asymmetry of Hudson Bay. *J Geophys Res: Oceans* **125**: e2019JC015756. DOI: http://dx.doi.org/10.1029/2019JC015756.

Kuzyk, ZA, Candlish, LM. 2019. *From science to policy in the Greater Hudson Bay Marine Region: An Integrated Regional Impact Study (IRIS) of climate change and modernization*. Québec, Canada: Univ Laval: 424. Available at https://arcticnet.ulaval.ca//pdf/media/IRIS_3_synthesis_to_print_rev1.pdf.

Kuzyk, ZA, Macdonald, RW, Stern, GA, Gobeil, C. 2011. Inferences about the modern organic carbon cycle from diagenesis of redox-sensitive elements in

Hudson Bay. *J Mar Syst* **88**: 451–462. DOI: http://dx.doi.org/10.1016/j.jmarsys.2010.11.001.

Landy, JC, Ehn, JK, Babb, DG, Thériault, N, Barber, DG. 2017. Sea ice thickness in the Eastern Canadian Arctic: Hudson Bay Complex and Baffin Bay. *Remote Sens Environ* **200**: 281–294. DOI: http://dx.doi.org/10.1016/j.rse.2017.08.019.

Lindström, G, Pers, C, Rosberg, J, Strömqvist, J, Arheimer, B. 2010. Development and testing of the HYPE (Hydrological Predictions for the Environment) water quality model for different spatial scales. *Hydrol Res* **41**: 295–319, DOI: http://dx.doi.org/10.2166/nh.2010.007.

Madec, G. 2008. NEMO ocean engine. *Note du Pôle de modélisation*, Institut Pierre-Simon Laplace (IPSL), France, 27, ISSN No: 1288–1619.

Masina, S, Storto, A, Ferry, N, Valdivieso, M, Haines, K, Balmaseda, M, Zuo, H, Drevillon, M, Parent, L. 2017. An ensemble of eddy-permitting global ocean reanalyses from the MyOcean project. *Clim Dyn* **49**: 813–841. DOI: http://dx.doi.org/10.1007/s00382-015-2728-5.

Myers, RA, Akenhead, SA, Drinkwater, K. 1990. The influence of Hudson Bay runoff and ice-melt on the salinity of the inner Newfoundland Shelf. *Atmos-Ocean* **28**(2): 241–256. DOI: http://dx.doi.org/10.1080/07055900.1990.964937.

Petrusevich, VY, Dmitrenko, IA, Niemi, A, Kirillov, SA, Kamula, CM, Kuzyk, ZZA, Barber, DG, Ehn, JK. 2020. Impact of tidal dynamics on diel vertical migration of zooplankton in Hudson Bay. *Ocean Science* **16**: 337–353. DOI: http://dx.doi.org/10.5194/os-16-337-2020.

Pierrejean, M, Babb, DG, Maps, F, Nozais, C, Archambault, P. 2020. Spatial distribution of epifaunal communities in the Hudson Bay System: Patterns and drivers. *Elem Sci Anth* (submitted).

Prinsenberg, SJ. 1984. Freshwater contents and heat budgets of James Bay and Hudson Bay. *Cont Shelf Res* **3**(2): 191–200. DOI: http://dx.doi.org/10.1016/0278-4343(84)90007-4.

Prinsenberg, SJ. 1986a. Salinity and temperature distribution of Hudson Bay and James Bay, in Martini, EP ed., *Canadian inland seas* (*Oceanography Series 44*). New York: Elsevier: 163–186.

Prinsenberg, SJ. 1986b. The circulation pattern and current structure of Hudson, in Martini, EP ed., *Canadian inland seas* (*Oceanography Series 44*). New York: Elsevier; 187–203.

Prinsenberg, SJ. 1988. Ice-cover and ice-ridge contributions to the freshwater contents of Hudson Bay and Foxe Basin. *Arctic* **41**(1): 6–11. DOI: http://dx.doi.org/10.14430/arctic1686.

Prinsenberg, SJ. 1991. Effects of hydro-electric projects on Hudson Bay's marine and ice environments. *Potential Environ Impacts Ser* 2, 8 pp, North Wind Inf Serv, Montreal.

Ridenour, NA, Hu, X, Jafarikhasragh, S, Landy, JC, Lukovich, JV, Stadnyk, TA, Sydor, K, Myers, PG, Barber, DG. 2019a. Sensitivity of freshwater dynamics to ocean model resolution and river discharge forcing in the Hudson Bay Complex. *J Mar Syst* **196**: 48–64. DOI: http://dx.doi.org/10.1016/j.jmarsys.2019.04.002.

Ridenour, NA, Hu, X, Sydor, K, Myers, PG, Barber, DG. 2019b. Revisiting the circulation of Hudson Bay: Evidence for a seasonal pattern. *Geophys Res Lett* **46**: 3891–3899. DOI: http://dx.doi.org/10.1029/2019GL082344.

Saucier, FJ, Dionne, J. 1998. A 3-D coupled ice-ocean model applied to Hudson Bay, Canada: The seasonal cycle and time-dependent climate response to atmospheric forcing and runoff. *J Geophys Res* **103**: 27689–27705. DOI: http://dx.doi.org/10.1029/98JC02066.

Saucier, FJ, Senneville, S, Prinsenberg, S, Roy, F, Smith, G, Gachon, P, Caya, D, Laprise, R. 2004. Modelling the sea ice-ocean seasonal cycle in Hudson Bay, Foxe Basin and Hudson Strait, Canada. *Clim Dyn* **23**: 303–326. DOI: http://dx.doi.org/10.1007/s00382-004-0445-6.

Schulze, LM, Pickart, RS. 2012. Seasonal variation of upwelling in the Alaskan Beaufort Sea: Impact of sea ice cover. *J Geophys Res* **117**: C06022. DOI: http://dx.doi.org/10.1029/2012JC007985.

Smith, CA, Compo, GP, Hooper, DK. 2014a. Web-based reanalysis intercomparison tools (WRIT) for analysis and comparison of reanalyses and other datasets. *Bull Amer Meteor Soc* **95**(11): 1671–1678. DOI: http://dx.doi.org/10.1175/BAMS-D-13-00192.1.

Smith, GC, Roy, F, Mann, P, Dupont, F Brasnett, B, Lemieux, J-F, Laroche, S, Bélair, S. 2014b. A new atmospheric dataset for forcing ice–ocean models: Evaluation of reforecasts using the Canadian global deterministic prediction system, *Q J R Meteorol Soc* **140**: 881–894. DOI: http://dx.doi.org/10.1002/qj.2194.

St-Laurent, P, Straneo, F, Barber, DG. 2012. A conceptual model of an Arctic sea. *J Geophys Res* **117**: C06010. DOI: http://dx.doi.org/10.1029/2011JC007652.

St-Laurent, P, Straneo, F, Dumais, J-F, Barber, DG. 2011. What is the fate of the river waters of Hudson Bay? *J Mar Syst* **88**: 352–361, DOI: http://dx.doi.org/10.1016/j.jmarsys.2011.02.004.

Straneo, F, Saucier, F. 2008. The outflow from Hudson Strait and its contribution to the Labrador Current. *Deep-Sea Res Pt I* **55**: 926– 946. DOI: http://dx.doi.org/10.1016/j.dsr.2008.03.012.

Walsh, JE, Chapman, WL, Shy, TL. 1996. Recent decrease of sea level pressure in the central Arctic. *J Clim* **9**: 480–486. DOI: http://dx.doi.org/0.1175/1520-0442(1996)009<0480: RDOSLP>2.0.CO;2.

How to cite this article: Dmitrenko, IA, Myers, PG, Kirillov, SA, Babb, DG, Volkov, DL, Lukovich, JV, Tao, R, Ehn, JK, Sydor, K, Barber, DG. 2020. Atmospheric vorticity sets the basin-scale circulation in Hudson Bay. *Elem Sci Anth*. 8: xx. DOI: https://doi.org/10.1525/elementa.049

Domain Editor-in-Chief: Jody W. Deming, University of Washington, Seattle, WA, USA

Associate Editor: Mary-Louise Timmermans, Yale University, New Haven, CT, USA

Knowledge Domain: Ocean Science

Part of an Elementa Special Feature: BaySys

Published: 00, 0000 **Accepted:** October 17, 2020 **Submitted:** May 14, 2020

ELEMENTA Science of the Anthropocene

Elem Sci Anth is a peer-reviewed open access journal published by University of California Press.

OPEN ACCESS